AGU PUBLICATIONS

Journal of Advances in Modeling Earth Systems

RESEARCH ARTICLE
10.1002/2014MS000384

Special Section:
The 2011-12 Indian Ocean Field Campaign: Atmospheric-Oceanic Processes and MJO Initiation

Mechanisms of convective cloud organization by cold pools over tropical warm ocean during the AMIE/DYNAMO field campaign

Zhe Feng[1], Samson Hagos[1], Angela K. Rowe[2], Casey D. Burleyson[1], Matus N. Martini[1], and Simon P. de Szoeke[3]

[1]Pacific Northwest National Laboratory, Richland, Washington, USA, [2]Department of Atmospheric Sciences, University of Washington, Seattle, Washington, USA, [3]College of Earth, Ocean, and Atmospheric Sciences, Oregon State University, Corvallis, Oregon, USA

Key Points:
- Intersecting cold pools trigger more clouds than isolated ones
- Intersecting cold pools produce larger clouds and closer spacing among them
- Larger clouds and closer spacing promote deeper convection

Correspondence to:
Z. Feng,
zhe.feng@pnnl.gov

Citation:
Feng, Z., S. Hagos, A. K. Rowe, C. D. Burleyson, M. N. Martini, and S. P. de Szoeke (2015), Mechanisms of convective cloud organization by cold pools over tropical warm ocean during the AMIE/DYNAMO field campaign, *J. Adv. Model. Earth Syst.*, *7*, 357–381, doi:10.1002/2014MS000384.

Received 5 SEP 2014
Accepted 16 JAN 2015
Accepted article online 28 JAN 2015
Published online 3 APR 2015

Abstract This paper investigates the mechanisms of convective cloud organization by precipitation-driven cold pools over the warm tropical Indian Ocean during the 2011 Atmospheric Radiation Measurement (ARM) Madden-Julian Oscillation (MJO) Investigation Experiment/Dynamics of the MJO (AMIE/DYNAMO) field campaign. A high-resolution regional model simulation is performed using the Weather Research and Forecasting model during the transition from suppressed to active phases of the November 2011 MJO. The simulated cold pool lifetimes, spatial extent, and thermodynamic properties agree well with the radar and ship-borne observations from the field campaign. The thermodynamic and dynamic structures of the outflow boundaries of isolated and intersecting cold pools in the simulation and the associated secondary cloud populations are examined. Intersecting cold pools last more than twice as long, are twice as large, 41% more intense (measured with buoyancy), and 62% deeper than isolated cold pools. Consequently, intersecting cold pools trigger 73% more convection than do isolated ones. This is due to stronger outflows that enhance secondary updraft velocities by up to 45%. However, cold pool-triggered convective clouds grow into deep convection not because of the stronger secondary updrafts at cloud base, but rather due to closer spacing (aggregation) between clouds and larger cloud clusters that form along the cold pool boundaries when they intersect. The close spacing of large clouds moistens the local environment and reduces entrainment drying, increasing the probability that the clouds further develop into deep convection. Implications for the design of future convective parameterization with cold pool-modulated entrainment rates are discussed.

1. Introduction

As rain drops descend into unsaturated air, they can evaporate, leading to a descent of cold air down to the surface. Once the cold air comes in contact with the surface, it spreads out horizontally, displacing the warmer ambient boundary layer air and forming cold pools. The dynamics associated with cold pools are an important mechanism of organizing convection because new convection could form when the surrounding warm boundary layer air is lifted by the expanding cold air. The boundary between the cold pool and warm boundary layer air is commonly referred to as the outflow boundary or gust front.

The "self-organization" of convection was first observed from space by *Purdom* [1976] who studied images from the first Geostationary Operational Environmental Satellite (GOES-1) over the U.S. and noted that storm-produced cloud boundaries oftentimes appeared as arc-shaped clouds in the satellite imagery. Later, *Purdom and Marcus* [1982] further classified storm generation mechanisms using several months of satellite imagery in the southeastern U.S. They showed that merging of outflow boundaries and intersections of gust fronts become an increasingly dominant convective triggering mechanism from early to late afternoon as the percentage of triggered convection from non-outflow-related local forcing steadily declines. Similar findings based on scanning weather radar observations were reported by *Wilson and Schreiber* [1986]. They found that the majority of intense storms east of the Colorado Rocky Mountains form along convergence lines of convective storm outflows. Using 3-D numerical models, *Droegemeier and Wilhelmson* [1985] found two types of convective clouds can be triggered by colliding outflow boundaries. One arises from ambient

air in the outflow collision region being "squeezed" out as the outflows collide, forcing some of the ambient air to be lifted to saturation and trigger convection. The other type results from low-level air being forced to rise up and over the cold pool due to a deflection by the pressure gradient force. They reported that the convective cloud updrafts of both types are virtually undiluted and originate from the near-surface region, suggesting that convection triggered by intersecting outflow boundaries could potentially further grow into deep convection.

The diurnal cycle of convection over land, especially the fact that peak deep convection frequency occurs several hours after the time of maximum solar heating (noon), has been linked to cold pools. Using a combination of ground-based radar and geostationary satellite observations during the Tropical Rainfall Measuring Mission-Large-Scale Biosphere-Atmosphere (TRMM-LBA) project to identify storm triggering mechanisms, *Lima and Wilson* [2008] found that small convective storms initiate early in the afternoon and produce small cold pools, which subsequently would merge with others to form larger cold pools with near-circular gust fronts. Subsequent storms were preferentially initiated along these gust front regions. They showed that lifting by isolated and colliding gust fronts accounts for up to 52% of new storms when large-scale forcing is weak.

The importance of cold pools for the transition from shallow to deep convection over land was also shown by *Khairoutdinov and Randall* [2006]. By switching off the evaporation of precipitation to suppress cold pool formation in their large eddy simulation (LES), they found that convection remains shallow even in the presence of large convective available potential energy (CAPE) and virtually no convective inhibition (CIN) in the environmental sounding. These results suggest that precipitation and cold pools are needed to generate thermals large enough to penetrate deep into the troposphere and support the growth of deep clouds. Similar results are also reported by *Böing et al*. [2012] using a different LES simulation. In a similar LES experiment conducted in a tropical oceanic environment, suppressing cold pools resulted in a roughly 50% reduction in shallow and congestus cloud amounts [*Khairoutdinov et al*., 2009]. Evidence for the organization of shallow convection by cold pool dynamics is also found in both observations and model simulations of open cells in marine stratocumulus clouds [*Terai and Wood*, 2013; *Wang and Feingold*, 2009] and trade-wind cumulus clouds [*Li et al*., 2014; *Zuidema et al*., 2011]. Collectively, these studies show that cold pools play an important role in the triggering of new convective clouds in a wide range of atmospheric environments.

Over the ocean, precipitation-driven cold pools contribute to the variability of ocean-atmosphere heat and moisture exchange. Using ship measurements over the tropical western Pacific ocean, *Chuda et al*. [2008] showed that surface latent and sensible heat fluxes are significantly enhanced around precipitating cloud systems due to increased wind speeds and drops in near-surface air temperature that result from cold pools. They estimated that the precipitating clouds are responsible for 41% and 10% enhancement of the sensible and latent heat fluxes, respectively. *Zipser* [1977] used aircraft measurements of a tropical squall line in the Caribbean to document the thermodynamic structures of the oceanic convective system in the lower troposphere. He found that near-surface temperature depressions in cold pools recover faster than that of water vapor. He hypothesized that mixing at the top of the mixed layer may be stronger than cold pool-enhanced surface latent heat fluxes, limiting the recovery of the near-surface moisture depression. This is similar to the slow moisture recovery observed in cold pools associated with trade wind cumulus [*Zuidema et al*., 2011].

Traditionally, convective triggering by cold pools has been largely attributed to the dynamical effect of lifting the boundary layer air along the outflow above a negatively buoyant CIN layer, generating free convection [e.g., *Böing et al*., 2012; *Khairoutdinov and Randall*, 2006; *Krueger*, 1988]. *Tompkins* [2001] proposed a different mechanism that attributes the triggering to thermodynamic processes. Using cloud-resolving model (CRM) simulations, he examined cold pools formed by isolated convective cells over a warm ocean and in a weak wind-shear environment. His results showed that new convective clouds are not formed when cold pools are at their maximum intensity (in terms of buoyancy) or when maxima in outflow depth and wind speed were observed, but rather after surface temperature has recovered via increased surface fluxes, reducing CIN, yet while moisture anomalies remain high in the environment. In these high CAPE, low CIN conditions, he proposed that any small disturbance could generate new convection. He therefore attributed the role of cold pools in the organization of convection in this environment to mainly thermodynamic mechanisms.

While the exact convective triggering mechanism of cold pools is still in debate, further questions pertaining to the fate of cold pool-triggered clouds need to be addressed. In particular, what causes deep convection to preferentially form along the edges of cold pools? Some recent studies have shed light on this issue. Using Lagrangian particle analysis to trace cumulus air parcels back to the subcloud layer in an LES simulation, *Böing et al*. [2012] showed that parcels' thermodynamic properties at cloud base differ very little from each other. However, they found a strong correlation between parcel detrainment height and cloud size at cloud base. They proposed that while clouds tend to form along cold pool outflow boundaries, the deepest clouds formed at the intersection of multiple cold pools due to the surrounding clouds that reduce the interaction with drier non-cloudy air. *Schlemmer and Hohenegger* [2014] reported that larger moist patches around cold pools support larger clouds, which are less affected by the entrainment of unsaturated air and, over time, become deeper. Through a series of experiments with varied environmental moisture and wind profiles, they showed positive correlations between precipitation, cold pool buoyancy, area of the moisture anomaly, and consequently larger and deeper clouds. This supports the "near-environment" hypothesis of *Böing et al*. [2012]. Similar relationships between entrainment rate and cloud size modulated by cold pools are found in other studies as well [e.g., *Khairoutdinov and Randall*, 2006; *Kuang and Bretherton*, 2006].

The resolution of traditional General Circulation Models (GCMs) is too coarse to resolve cold pool processes and must rely on parameterization to capture their effects. Despite their recognized importance, cold pools are generally not explicitly treated in modern GCMs. This is partially due to a lack of understanding of which aspects of cold pool dynamics are most important for organizing convection. *Qian et al*. [1998] parameterized cold pools as density currents induced by downdrafts, with gust front-triggered updrafts related to the propagation speed of the wake current. They showed that their model could produce reasonable cold pool depths, sizes, and recovery times comparable to observations in the tropics. The effects of cold pools on enhancing the surface latent and sensible heat fluxes through wind gustiness were parameterized as functions of precipitation or updraft and downdraft mass fluxes generated by deep convective cells [*Redelsperger et al*., 2000; *Zeng et al*., 2002]. The dynamical effects of cold pools were parameterized by *Rio et al*. [2009] in an effort to better represent precipitation-driven cold pool lifting effects on the diurnal cycle of convection over land. They showed in a single column model that the parameterized lifting due to cold pools, which depended on virtual potential temperature differences between downdrafts and the environment, reinforces convection, and maintains active convective precipitation until early evening. This extension of convective lifetimes could potentially alleviate the long-standing problem of biases in the diurnal cycle of precipitation in convective parameterizations. Since then, a "convective wake" parameterization has been developed by *Grandpeix and Lafore* [2010], extensively tested in 1-D [*Grandpeix et al*. 2010] and implemented in the 3-D Laboratoire de Météorologie Dynamique Model with Zoom Capability (LMDZ) that participated in Coupled Model Intercomparison Project Phase 5 (CMIP5) [*Hourdin et al*., 2013; *Rio et al*., 2013].

While the above literature review is by no means exhaustive, proposed mechanisms through which cold pools can trigger deep convection fall into one of two categories, namely their thermodynamic and dynamic effects. Moreover, while many previous studies have argued that the interaction of cold pools tends to promote stronger and more organized convection than isolated ones, no quantitative results have been reported on the relative contributions of isolated and intersecting cold pools. The following questions remained unanswered: What mechanisms cause deep clouds to form at the edge of cold pools? Is it subcloud processes? Are thermodynamic or dynamic influences the dominant factor? How does the free-tropospheric environment affect newly triggered convection? Last, due to the difficulty in observing cold pools and their interactions, most of the previous studies rely on using idealized model simulations. The properties and impacts of the simulated convective clouds and cold pools compared to those in nature are unclear.

All the above-mentioned issues warrant further investigation of cold pool dynamics and their interactions with deep convection. In this study, we examine the proposed mechanisms of convective organization by cold pools over a warm tropical ocean using high-resolution regional model simulations. We will evaluate the simulated cold pool properties using data from the 2011 Atmospheric Radiation Measurement (ARM) Madden-Julian Oscillation (MJO) Investigation Experiment/Dynamics of the MJO (AMIE/DYNAMO) field campaigns [see *Yoneyama et al*., 2013 for details]. During the field campaign, three active MJO periods characterized by enhanced rainfall and organized Mesoscale Convective Systems (MCSs) were observed [*Rowe and Houze*, 2014a].Between these periods, suppressed conditions prevailed, which were characterized by

shallower convection and less overall rainfall. Rowe and Houze (submitted manuscript, 2014) found that nonprecipitating clouds observed by the S-PolKa radar organized as boundary layer rolls during the early parts of the suppressed periods. They showed that as these clouds began to precipitate, the cold pools they produced began to organize the cloud populations. As the cold pools intersected, new convection would form along these boundaries and eventually produce their own cold pools. This led to a pattern of increased numbers of cells and overall deeper convection as the active MJO phases approached, suggesting that there may be a positive feedback between cold pools and the transition from suppressed to active MJO phases. While some details of this transition from boundary layer features to deep convection are provided by Rowe and Houze (submitted manuscript, 2014), overall characteristics of the cold pools observed during AMIE/DYNAMO and how they facilitate development of deep convection are discussed in this study.

In this study, the relative contributions to convective triggering of isolated and intersecting cold pools will be quantified. Questions related to what aspects associated with cold pool dynamics lead to the development of deep convection will also be addressed. The paper is organized as follows: section 2 presents the observations collected during the AMIE/DYNAMO field campaign that are used to characterize precipitation-driven cold pools; section 3 describes the model simulation setup and analysis methods to identify and track cold pools along with the convective clouds they trigger; the cold pool characteristics and physical changes of the environment they induce are presented in section 4; in section 5, we investigate the mechanisms of convective cloud triggering and organization. A summary of our findings and their implications for parameterization are provided in section 6.

2. AMIE/DYNAMO Observations of Cold Pools

2.1. S-PolKa

The S-PolKa radar, located on the Addu Atoll in the Maldives (0.69°S, 73.15°E), operated from 1 October 2011 to 15 January 2012 during the AMIE/DYNAMO field campaign. The scanning strategy was a 15 min cycle that included 360° azimuthal surveillance scans with a starting elevation angle of 0.5°. While quality control efforts were a priority for rainfall estimates, clutter was retained in the data for the purposes of this study to aid in identification of cold pool boundaries. We use the lowest 0.5° surveillance elevation scans to identify cold pools. For more information about the scanning strategy and quality control of the S-PolKa data, see *Rowe and Houze* [2014a].

In addition to detecting precipitation echo, S-PolKa's high sensitivity allowed for nonprecipitating echoes to be observed [*Feng et al*., 2014]. Clear-air returns in the S-PolKa radar observations are observable as the Bragg scatter that results from moisture gradients in the atmosphere [e.g., *Davison et al*., 2013]. As convection produced rainfall and subsequent cold pools, the drying of the boundary layer air within cold pools created echo-free regions, which appear as "holes" in the background Bragg scatter (Figure 1). Along the edges of these echo-free regions were localized areas of slightly enhanced radar reflectivity (approaching 0 dBZ), which marked the leading edge of the cold pools. These boundaries could be tracked as single entities until they reached ranges, usually beyond 100 km, too far from the radar to identify their outer edges. More commonly these boundaries would intersect, either serving as a focal point for new convective initiation or merging to form larger cold pools, at which point the original boundaries were no longer discernable.

Objectively identifying these cold pool boundaries is a challenge as they are not always clearly defined and are not characterized by distinct polarimetric radar signatures. In suppressed MJO periods when convection was relatively more isolated and these circular cold pool features were more prominent, a subjective approach can be used to identify boundaries of echo-free regions in each radar scan until they were beyond the radar range or merged with nearby cold pools. To distinguish between cold pools and other clear-air features (such as the open cells described by J. H. Ruppert, Jr. and R. H. Johnson, Cumulus moistening, the diurnal cycle, and initiation of the Madden-Julian oscillation during DYNAMO, submitted to *Journal of Atmospheric Sciences*, 2014), a boundary was only tracked if it could be traced back to a precipitating cell. For the three suppressed periods (early October, November, and December 2011), this method identified a total of 52 cold pools. These cold pools were manually tracked to determine their maximum diameter (to the nearest 5 km) and duration. Because of the complexity of these features and the difficulty in distinguishing individual cold pools when they merge with nearby ones, isolated and intersecting cold pools were not

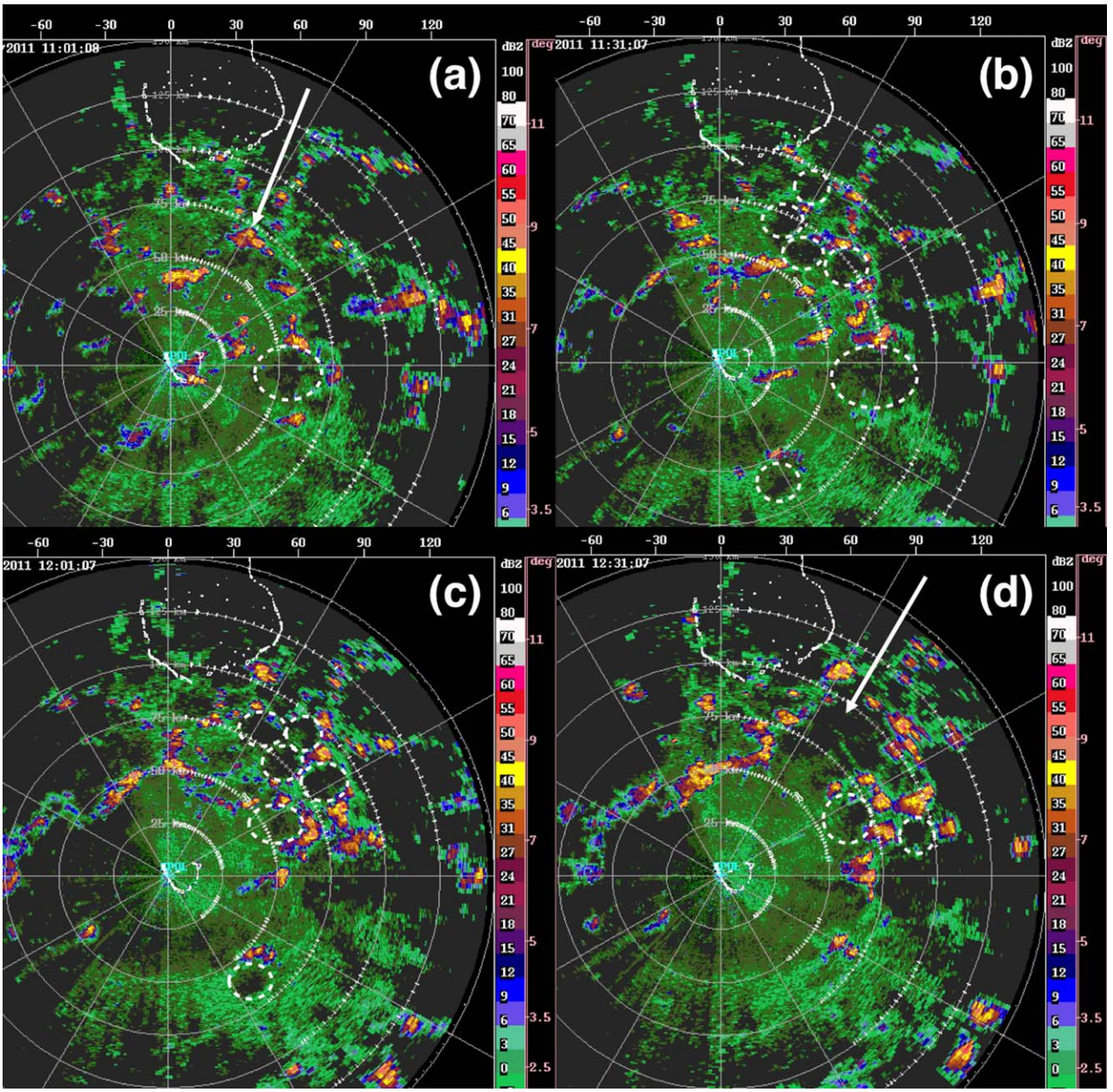

Figure 1. A sequence of S-PolKa radar-observed convective cells and cold pools (subjectively identified by white-dashed circles) over the tropical Indian Ocean on 10 October 2011 at (a) 1100 UTC, (b) 1130 UTC, (c) 1200 UTC, and (d) 1230 UTC. The S-Pol radar was deployed on Addu Atoll, Maldives during the 2011 AMIE/DYNAMO field campaign. Each concentric solid white circle increases by 25 km and the outer most circle marks the 150 km maximum range of the radar.

separated for the S-PolKa data. Cold pool characteristics observed by S-PolKa were similar for each of the three suppressed periods; therefore, we include all of the tracked cold pools from S-PolKa in this study to increase the sample size (N = 52).

An example of the S-PolKa-observed interaction between cold pools and convection is shown in Figure 1 for 10 October 2011 with scans (a-d) separated by 30 min. Sounding data showed a weak southwesterly wind in the boundary layer (0–2 km) with a daily average wind speed of around 6 m s^{-1}, and a 3 m s^{-1} wind difference between 1 and 3 km. At 1100 UTC (Figure 1a), numerous convective cells can be seen, particularly in the northeast sector of the radar domain. A few of the many convective cells and boundaries present will be discussed to demonstrate the tracking method and the interaction of cold pools. An

example of an echo-free region associated with a cold pool is identified due east of S-PolKa (Figure 1a, marked by a white dashed circle). At 1130 UTC (Figure 1b), this cold pool slightly expanded and moved farther east with the mean low-level flow. To show an example of a cold pool tracked from its parent convection, the arrow in Figure 1a points to a precipitating convective cell that left behind a cold pool at 1130 UTC. Nearby at this time are other cold pools produced by neighboring convective cells. Also at this time, a small cell 50 km to the southeast of S-PolKa created an isolated cold pool with no apparent interaction with any nearby boundaries, highlighting the range of cold-pool scenarios observed by the radar. Moving forward to 1200 UTC (Figure 1c), the echo-free region associated with the isolated cold pool in the southeast is still clearly identifiable. However, the cold pool that was being tracked directly to the east of the radar is no longer easily detectable at this time. Further to the northeast of S-PolKa, numerous small intersecting cold pools remained and focal points of enhanced convection can be seen along their boundaries. By 1230 UTC (Figure 1d), these cold pools had merged (as indicated by the arrow) and their individual boundaries became indistinguishable.

Figure 1, a representative example during the transition from suppressed to active phases of the MJO, illustrates the difficulty of separating isolated and intersecting cold pools observed in the radar data. While the echo-free region to the northeast of S-PolKa at 1230 UTC appears as one single cold pool (indicated to by the arrow in Figure 1d), when tracing it back in time it is clear that it was formed by the merger of several cold pools. These intersecting boundaries produced strong convective cells compared especially to the more isolated cold pool to the southeast that did not produce any new convection. The number and intensity of new convective cells forming along these cold pools are discussed in more detail in Rowe and Houze (submitted manuscript, 2014) whereas the maximum sizes and lifetimes of the visually tracked cold pools in the S-PolKa observations will be statistically compared to model simulated cold pools in section 4 of this paper.

2.2. R/V Revelle

Near-surface meteorology measurements from the *Revelle* research vessel (*R/V*), stationed to the east (0°N, 80.5°E) of S-PolKa during AMIE/DYNAMO, are used to examine the properties of cold pools as they pass over the ship. We use the *R/V Revelle* measurements from 12 November to 25 November 2011, during which the ship was stationed close to the equator near 80°E. This location was slightly outside of our model simulation domain (section 3) for the time period examined, thus potentially leading to differences between the observations and the model in the frequency and dynamic characteristics of cold pools. To limit the sensitivity to these potential differences, our analysis focuses on *changes* to the near-surface atmosphere during the passage of colds pool rather than absolute values.

We used the *R/V Revelle* measurements rather than those from the ARM Mobile Facility (AMF) deployed at Addu Atoll near S-PolKa because the ship measurements of the near-surface air temperatures are more representative of the oceanic surface environment than those collected on land at the atoll. Surface air temperatures in the AMF data set had a larger amplitude diurnal cycle. Additionally, surface flux measurements over the ocean were only made by the ship. Near-surface air temperature time series are filtered using a square Haar wavelet filter with a window width of $\pm$20 min [*Hagos et al*., 2014b], and the passage of a cold pool is defined as a temperature decrease larger than 0.5°C in the filtered temperature time series. Statistical comparisons of the near-surface properties during passage of cold pools between the *R/V Revelle* measurements and model simulation will be presented in the next section.

3. Model Setup and Analysis of Cold Pools

3.1. Model Configuration

We use the Advanced Research Weather Research and Forecasting (WRF) model V3.4.1 and a domain size of 1000 km $\times$ 500 km centered on Addu Atoll (Figure 2). The model horizontal grid spacing is 500 m with 40 vertical layers extending up to 19 km. To better resolve cold pools, the vertical grid spacing is 50 m below 500 m, then gradually coarsens to 500 m between 2 and 10 km, and finally 1 km spacing above 10 km. The microphysics scheme used is a modified Thompson scheme [*Thompson et al*., 2008], where raindrop self-collection efficiency is reduced and raindrop break-up efficiency is enhanced. *Hagos et al*. [2014b] show that simulated cold pool frequency is related to the microphysics schemes used in the model. They found that increasing the raindrop break-up efficiency reduces the reflectivity bias in the simulated

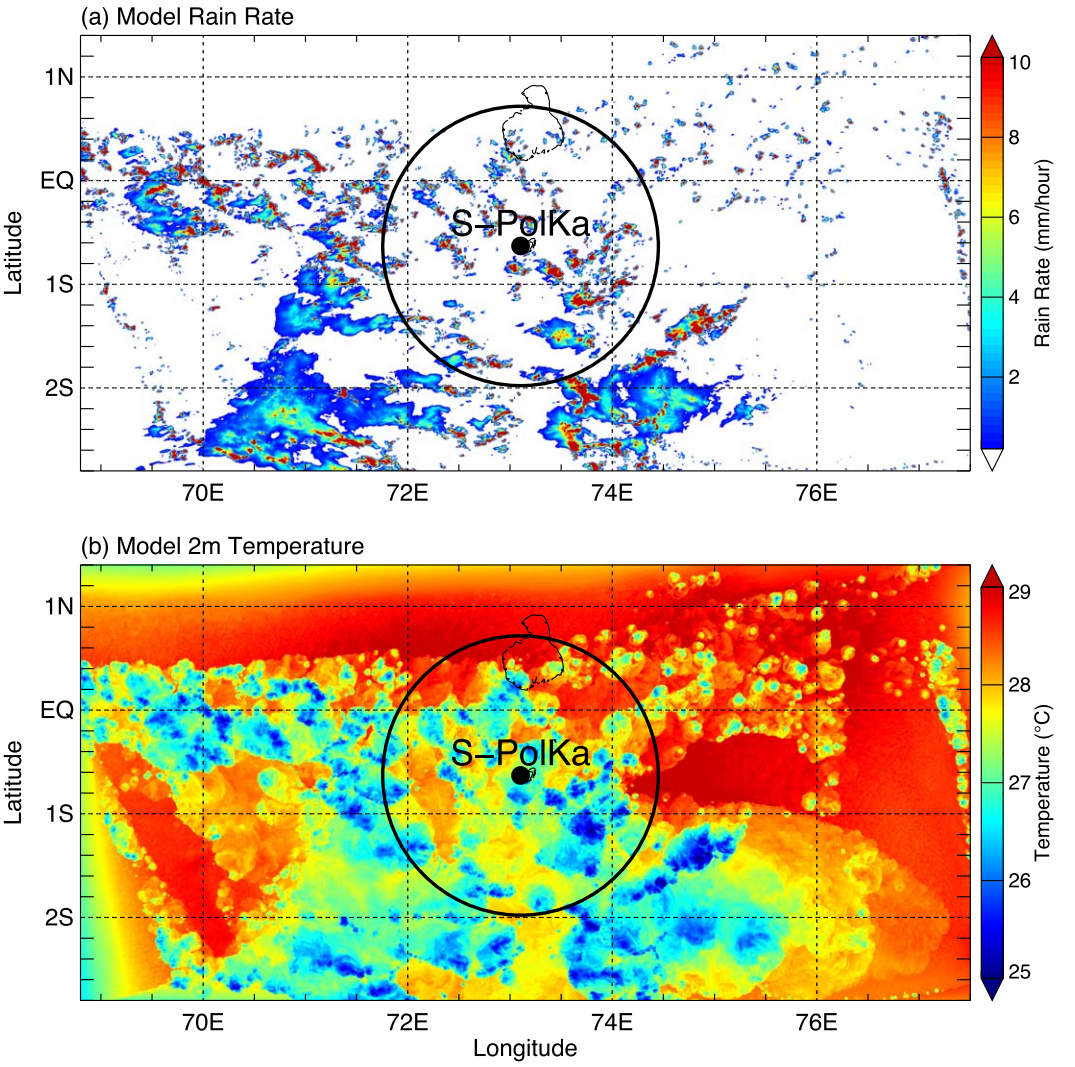

Figure 2. Model domain with a snapshot of (a) surface rain rate and (b) temperature at 2 m above surface at 2200 UTC on 15 November 2011. The model domain centers at Addu Atoll where the S-PolKa radar was deployed, and the circle marks the 150 km S-Pol maximum range.

convective cells, increases cold pool frequency, and results in better overall comparisons with observations. The modification of the Thompson scheme in this paper follows that implemented by *Hagos et al.* [2014b]. The simulation is run for the first 20 days of November 2011. This corresponds to the transition period from the suppressed to the active phases of the November MJO episode [*Yoneyama et al.*, 2013]. Forcing and SSTs from ERA-Interim reanalysis are applied at the lateral boundary of the domain and are updated every 6 h. Details of the model setup are given in Table 1. For the simulation setup in this study, the vertical grid spacing in the boundary layer is 50 m, much smaller than the horizontal grid spacing (500 m). Thus, we use 1-D PBL scheme that neglects the horizontal advection of turbulent kinetic energy.

Table 1. Model Setup

Simulation Period	1–20 November 2011
Lateral and surface forcing	ERA-Interim 6 hourly reanalysis
PBL scheme	Mellor-Yamada-Janjic [*Janjic*, 2002]
Surface scheme	Monin-Obukhov-Janjic [*Janjic*, 2002]
Long-wave radiation scheme	RRTMG [*Iacono et al.*, 2000]
Short-wave radiation scheme	[*Dudhia*, 1989]
Microphysics Raindrop self-collection (break-up) efficiency If $D > 50$ μm, $E_c = \alpha(2 - \exp(2.3 \times 10^3 (D - D_{th})))$	[*Thompson et al.*, 2008] $\alpha = 0.5$ (default $\alpha = 4.0$)

Figure 2a shows a snapshot of the model precipitation rate for a representative scene during the November MJO. This model, with a relatively large

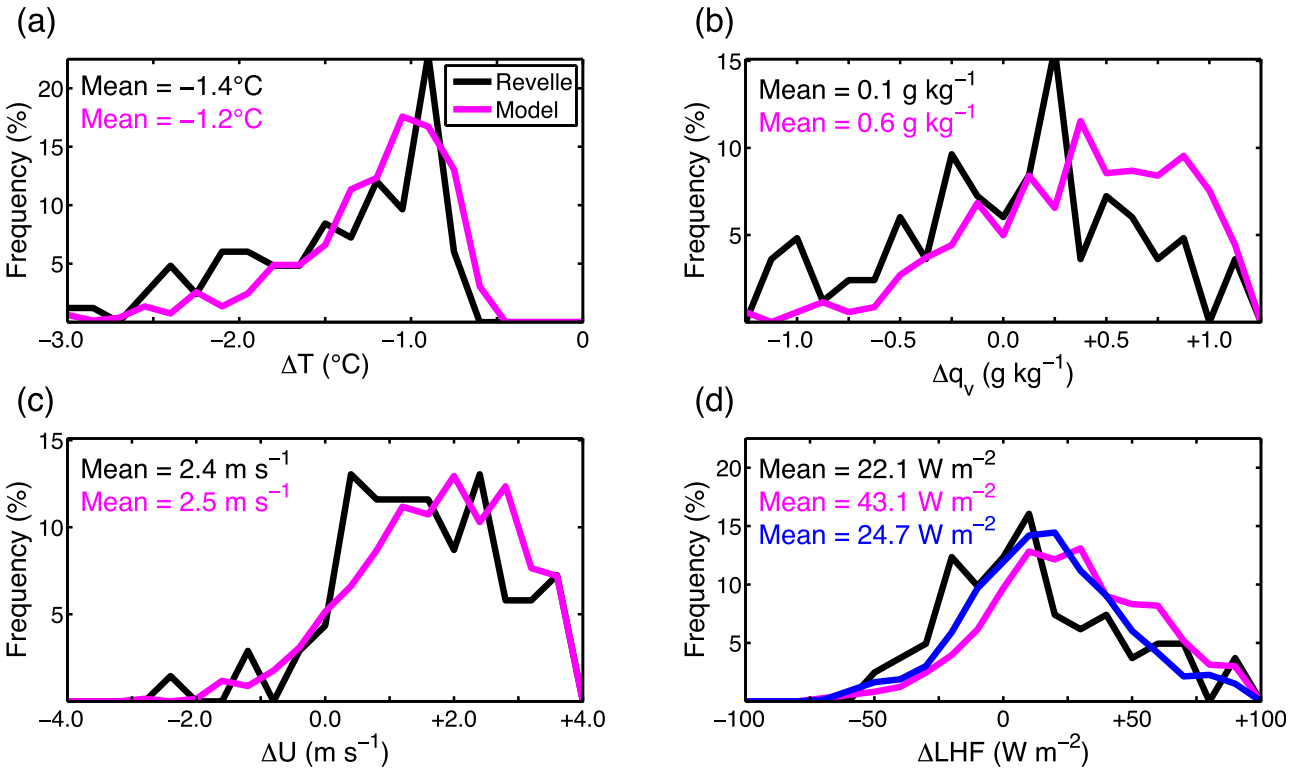

Figure 3. Probability density functions of near-surface thermodynamic changes during the passage of cold pools from the *R/V Revelle* observations (black) and the model output (magenta) for (a) 2 m temperature (minimum within the cold pool – maximum before), (b) 2 m water vapor mixing ratio (maximum within the cold pool – minimum before), (c) 10 m wind speed (maximum within the cold pool – minimum before), and (d) surface latent heat flux (mean within the cold pool – mean before). The blue line in Figure 3d is calculated from the model output using the COARE 3.0 algorithm, which is used to calculate fluxes in the *R/V Revelle* data set.

domain, is able to simulate a wide spectrum of convective precipitation, ranging from small isolated cells to sub-MCSs and MCSs. These span the range of observed convective cloud populations during this period of AMIE/DYNAMO [*Rowe and Houze*, 2014a; *Zuluaga and Houze*, 2013]. Figure 2b shows that precipitation-induced cold pools can reduce the warm oceanic near-surface temperature by several degrees. The gradient of background temperature near the western/northern edge of the domain (~1°C) is a result of the WRF model adjusting to the boundary conditions given by the ERA-Interim reanalysis. As discussed in more details in section 3.4, cold pools that touch the edge of the boundary during their lifetimes are excluded from our analysis. In general, near-surface temperature from the model simulation is about 1.4°C lower than the ERA-Interim reanalysis, but compares well with the *R/V Revelle* observations, suggesting that the high-resolution model is able to better represent the cooling effect of cold pools than their representations in the ERA-Interim reanalysis.

3.2. Comparison With Observed Cold Pool Properties

To compare with the *R/V Revelle* observations, the WRF simulation is sampled at a total of 24 fixed locations spaced 1° apart in the region between 2°S–1°N and 70°–75°E, yielding 11,520 h of independent time series. We used the same filtered temperature time series method to identify cold pools at each of the 24 locations. Figure 3 shows the probability density function (PDF) of the changes in near-surface temperature, water vapor mixing ratio, wind speed, and latent heat flux during the passages of cold pools. The simulation generates cold-pools that produce decreases in temperature and increases in water vapor mixing ratio, wind speed, and latent heat flux which agree reasonably well with the observations. Cold pools detected in the AMF data set have similar properties (not shown), meaning that the cold pools that passed over *R/V Revelle* were physically consistent with those near the location of the S-PolKa radar.

The model simulation has a positive bias in the change of water vapor and latent heat flux across cold pool boundaries likely due to the boundary layer and surface schemes used. Surface fluxes in the *R/V Revelle* data set were computed using the COARE 3.0 algorithm [*Fairall et al*., 2003], which is a bulk flux algorithm used to estimate surface fluxes from time series of wind speed, temperature, moisture, and the gradients of each variable between the sea-surface and the lowest layer of the atmosphere. While the COARE algorithm calculates the fluxes using Monin-Obukhov Similarity Theory, it also incorporates other atmospheric properties such as wave height and boundary layer depth. When we use the COARE algorithm to calculate fluxes in the model output, the mean difference in latent heat flux across cold pool boundaries is reduced by ~42% (blue line in Figure 3d). This suggests that part of the differences is related to variations in the way that the fluxes were calculated and the background latent heat flux distributions. Nevertheless, this comparison increases our confidence in the model results. The simulation is able to represent observed cold pool properties and convective cloud populations [see *Hagos et al*., 2014b for a more detailed model evaluation] reasonably well during the field campaign.

3.3. Identification of Cold Pools and Triggered Convection

To identify the spatial structure of cold pools in the simulation, we follow the method by *Tompkins* [2001] using buoyancy (b; m s^{-2}), which is defined as:

$$b=\frac{g(\theta_p-\bar{\theta}_p)}{\bar{\theta}_p} \tag{1}$$

where g is the acceleration due to gravity, and the overbar indicates a running mean value from a 100 km × 100 km region centered on a given point. Virtual potential temperature (θ_p; K) is defined as:

$$\theta_p=\theta(1+0.608q_v-q_{cloud}-q_{rain}) \tag{2}$$

where θ is potential temperature, and q_v, q_{cloud}, and q_{rain} are the mass mixing ratios of water vapor, cloud condensate, and rain water, respectively. Previous studies using CRM or LES models were conducted over relatively small horizontal regions with domain sizes ranging from 60 to 200 km, [e.g., *Böing et al*., 2012; *Khairoutdinov et al*., 2009; *Khairoutdinov and Randall*, 2006; *Tompkins*, 2001], and therefore their background value can be defined as the mean value across the entire domain. Because the simulation domain used in this study is significantly larger compared to those in previous studies, we obtain anomalies by subtracting the background value for a 100 km × 100 km subdomain. Cold pool intensity (B; m s^{-1}) is calculated using the vertical integral of buoyancy following *Bryan and Parker* [2010], which follows *Rotunno et al*. [1988]:

$$B=\sqrt{-2\int_0^h b\,dz} \tag{3}$$

where b is buoyancy (equation (1)), and h is the depth of cold pool, defined as the height at which b first exceeds −0.003 m s^{-2}.

To assess the spatial extent of cold pools, we used a buoyancy threshold of less than −0.003 m s^{-2} in the lowest model height (50 m) to contiguous areas belonging to a single cold pool. By comparison, *Tompkins* [2001] used a threshold of −0.005 m s^{-2}. The depth of cold pools at each grid point is then defined as the first vertical level (from bottom up) where buoyancy exceeds this threshold (i.e., no longer negatively buoyant). We note that by using the buoyancy at the lowest model height, the minimum depth of cold pools required in the analysis is 50 m. In addition, cold pools with weaker near-surface (50 m) buoyancy signatures but more intense buoyancy above may not be captured by this methodology. A different cold pool definition using the vertically integrated buoyancy field from surface to the top of the cold pool [e.g., *Grandpeix and Lafore*, 2010] may alleviate this issue. However, as we will show in section 5, most of the cold pools that produce deeper secondary convection tend to be stronger, neglecting the weaker cold pools should not affect our conclusions.

Once buoyancy in each grid point in the model is calculated, contiguous cold pool grid points are identified. Since one of our objectives is to quantify the relative contribution to convective triggering of isolated and intersecting cold pools, we apply a *watershed* technique [*Dougherty*, 1992] to identify these two groups of cold pools from the buoyancy field. The watershed technique segments a given 2-D data field into regions, analogous to "watersheds" or catchment basins in topography, and marks their boundaries. Similar applications of this technique have been used to perform cloud classification for precipitation retrieval algorithms

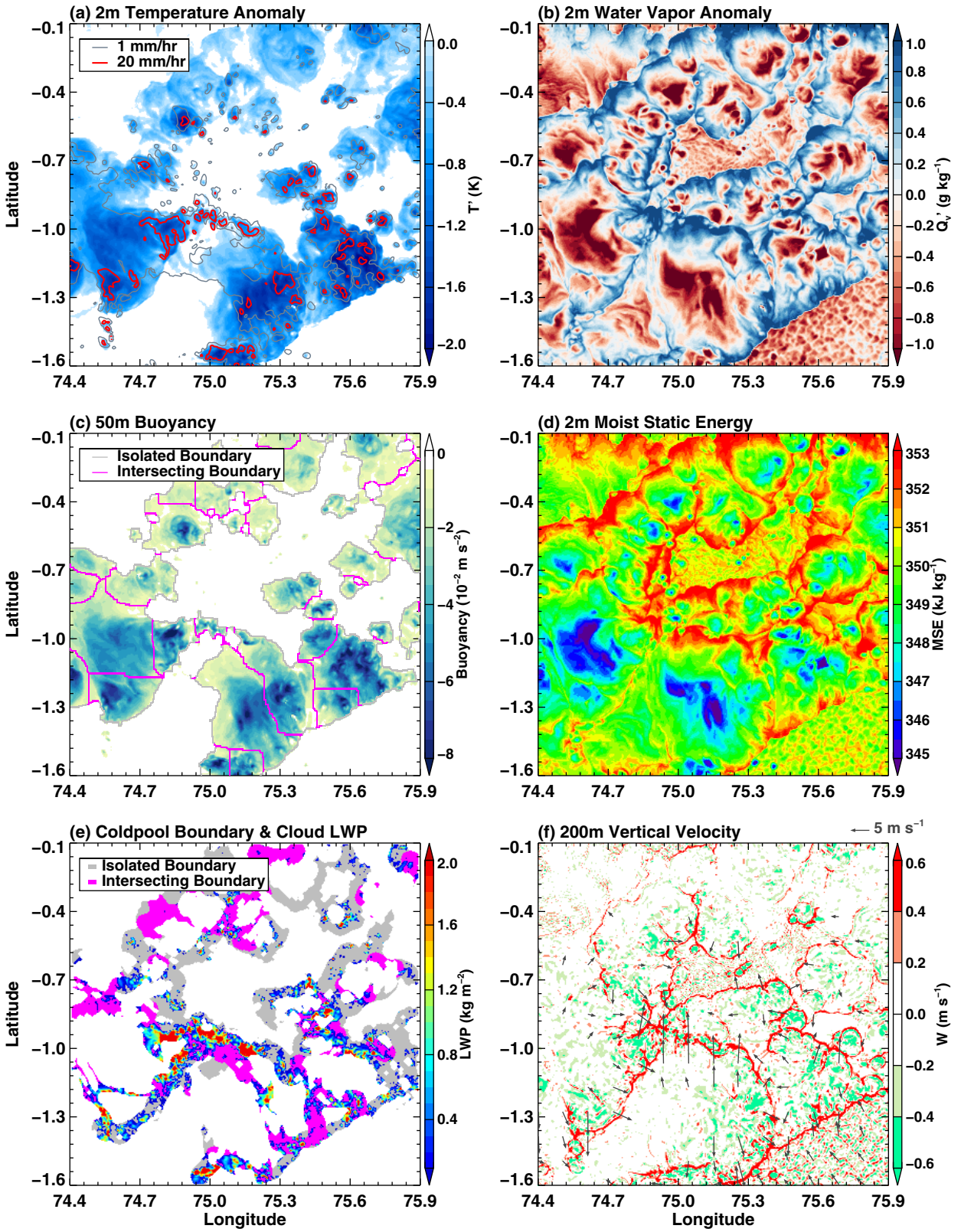

Figure 4. Snapshot of the simulation in an area with intersecting cold pools from 1730 UTC on 11 November 2011. Roughly 1/18 of the total model domain area (Figure 2) is shown. (a) 2 m temperature anomaly (shaded) and precipitation rate (contour), (b) 2 m water vapor anomaly, (c) 50 m buoyancy, (d) 2 m moist static energy, (e) cold pool boundaries and cloud LWP, and (f) 200 m vertical velocity (shaded) and 10 m wind (arrows show wind speeds > 2 m/s). Gray (magenta) lines in Figure 4c are nonintersecting (intersecting) cold pool boundaries, respectively. Gray (magenta) areas in Figure 4e are expanded from the boundaries in (c) to an 8 km wide area. See text for more details.

using satellite infrared images [*Hong et al*., 2004] and to identify organized mesoscale cellular convective cells in stratocumulus clouds [*Martini et al*., 2014]. A minimum threshold area of 1 km^2 (four contiguous grid points) is required for a cold pool to be identified.

Figure 4 illustrates an example of applying the watershed technique to identify individual cold pools in our simulation. Near-surface temperature (Figure 4a) and water vapor (Figure 4b) anomalies reveal several distinct cold pools produced by convective precipitation (rain rate $>$ 20 mm h^{-1}). Figure 4c shows the associated buoyancy and the individual cold pool boundaries defined by the watershed algorithm. A patch of negative buoyancy encompassed by a closed contour is considered a single cold pool. The gray contours outline the isolated (exterior) boundaries between cold pools and the environment, and the magenta contours are the intersecting (interior) boundaries between different cold pools. The near-surface moist static energy, vertical velocity at 200 m height, and surface wind are displayed in Figures 4d and 4f. Cold pool boundaries defined by the watershed technique closely match the locations of secondary updrafts, which typically occur along the cold pool outflow boundaries and have been shown to promote the triggering of new convection.

The example in Figure 4 shows that strong cold pools are usually associated with intense precipitation (Figure 4a) and downdrafts (Figure 4f). The center of a cold pool is characterized by colder and drier air that has significantly lower moist static energy than the edge (Figure 4d), consistent with previous studies [*Böing et al*., 2012; *Khairoutdinov and Randall*, 2006; *Tompkins*, 2001]. Such a water vapor structure is also found in cold pools from coupled ocean-atmosphere LES simulations representative of convection in AMIE/DYNAMO (E. D. Skyllingstad and S. P. deSzoeke, Cloud-resolving large-eddy simulation of tropical convective development and surface fluxes, submitted to *Monthly Weather Review*, 2014). When the watershed boundaries (Figure 4c) are combined with a water vapor anomaly, we can identify cold pool boundary region and the clouds triggered within. To accomplish this, the two types of watershed boundaries (Figure 4c, isolated (gray); intersecting (magenta), both only 1 grid point (500 m) in width) are expanded to an 8 km wide area. Within this expanded area, if the water vapor anomaly is positive, it is defined as corresponding cold pool boundaries (gray and magenta shading in Figure 4e), and the clouds (cloud liquid water path (LWP) $>$ 10 g m^{-2}) in these regions are considered convective clouds triggered by the cold pools (Figure 4e).

We chose a moderate-width and a low-LWP threshold to encompass most of the clouds that developed in the vicinity of cold pool boundaries without expanding too far outwards, where influence from the cold pools may no longer be relevant. Reducing the boundary width area and/or increasing the LWP threshold, both of which result in smaller boundary regions and clouds, does not significantly change our findings.

Most of the previous studies did not attempt to explicitly identify cold pool boundaries, possibly due to the complicated nature of intersecting cold pools. For example, *Schlemmer and Hohenegger* [2014] simply attribute clouds that formed in all the positive moist anomaly ($q_v > 5$ g kg^{-1}) area in their simulation to be caused by cold pools. While the boundary layer humidity in the vicinity of active convection can be largely modulated by cold pool outflows, in a simulation with realistic forcing such as the one in this study, other factors (e.g., large-scale convergence, advection, surface evaporation, etc.) could also influence the moisture field away from the cold pools. Further, the dynamical impact of outflow lifting in our simulation appears to be usually within a few kilometers from the cold pool boundary. Therefore, we argue that our approach better captures the convection that is triggered by processes occurring near the cold pool outflow edges. As seen in Figures 4e and 4f, the cold pool boundaries defined by our approach overlap with the updrafts along the cold pool edges. Examination of many other scenes with intersecting cold pools at different times and locations in our simulation shows similar patterns. This suggests that our approach is effective in capturing the triggering of convective clouds along the cold pool outflow boundaries.

The identification of isolated and intersecting cold pool boundaries also allows us to compare the relative amounts of convective clouds triggered by each. Anecdotally in the example shown in Figure 4, more clouds formed along the intersecting boundaries than isolated boundaries. Figure 5 shows a sequence of snapshots (separated by 10 min of simulation time) containing an example of new convection forming over colliding outflow boundaries. Two outflow boundaries (one propagating eastward and the other northward) associated with clear updraft bands collide around 1720 UTC and a large cloud cluster forms at the point of collision about 20–30 min later. The cloud cluster subsequently produces a large area of intense precipitation (rain rate $>$ 20 mm h^{-1}) and strong downdrafts, which creates its own cold pool that eventually

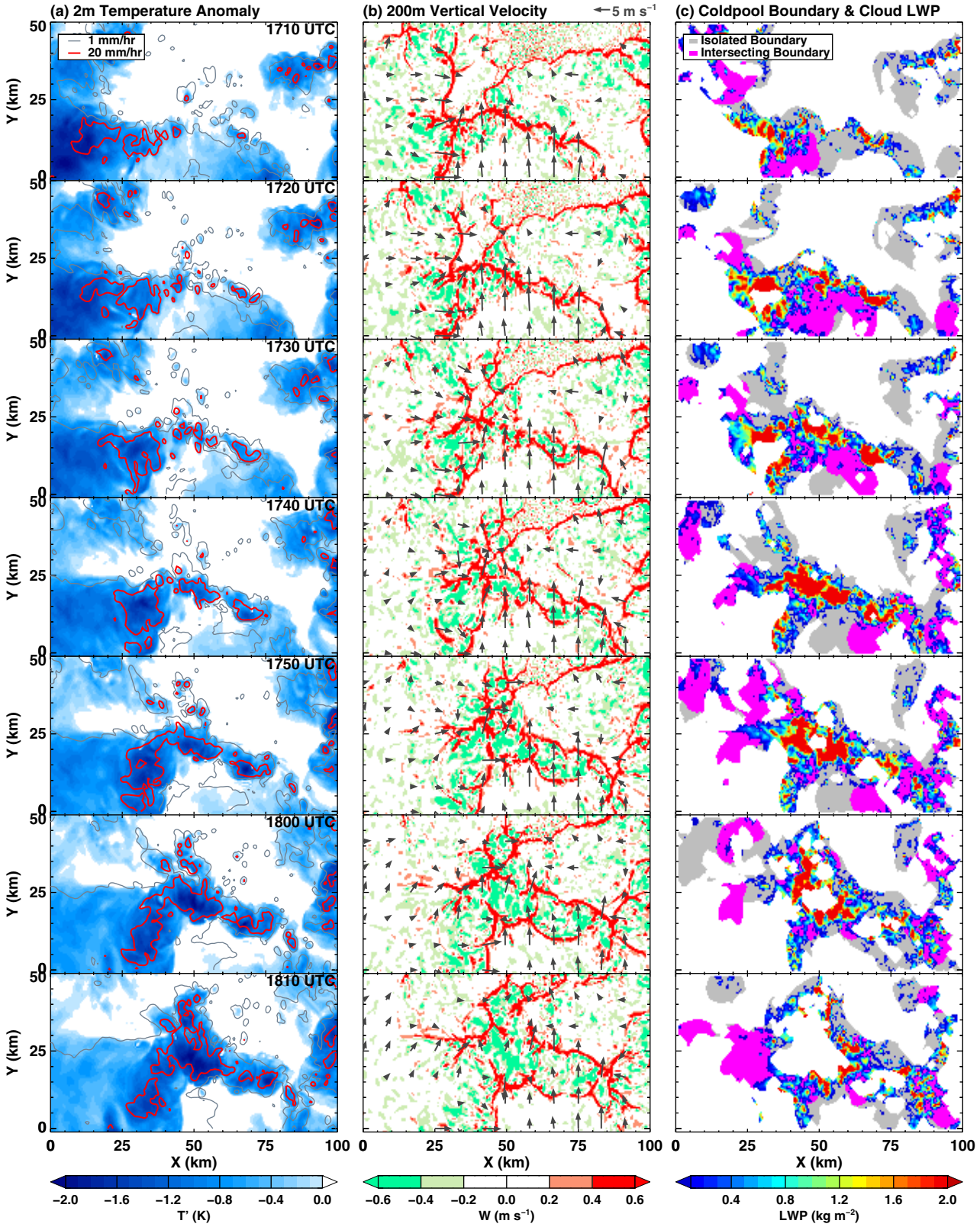

Figure 5. An example of a large cloud cluster formed at intersecting cold pool boundaries. Each row is a snapshot from a 10 min output, the columns from left to right are: (a) 2 m temperature anomaly (shaded) and rain rate (contour), (b) 200 m vertical velocity (shaded) and 10 m wind (arrows show wind speeds > 2 m/s), and (c) cold pool boundaries and cloud liquid water path, respectively.

spreads out, triggering new convection along its edges. Such a positive feedback between precipitation, downdrafts, cold pools, and new convection qualitatively follows the pattern observed by S-PolKa during suppressed MJO conditions (Rowe and Houze, –submitted manuscript, 2014).

3.4. Tracking of Cold Pools

An automated tracking algorithm is applied to the cold pools defined in the previous section in order to compare the triggering mechanisms associated with isolated and intersecting cold pools. The algorithm has been developed and used in previous studies for cloud tracking [*Feng et al*., 2012; *Hagos et al*., 2013]. It was modified in this study for application to cold pools. The tracking is based on a simple approach where overlapping objects between two consecutive frames are considered continuations of the same object. Tracking is performed by comparing consecutive 10 min periods of simulation output. If a cold pool overlaps more than 50% of its area with a cold pool in the previous scene, it is considered to be the same cold pool. Merging and splitting of cold pools in each time step are tagged. Merging occurs when two or more cold pools with distinct negative buoyancy centers collide and become one. Splitting occurs when two or more buoyancy centers emerge from new downdrafts within a single cold pool. In the case of merging, the largest of the merging cold pools is considered a continuation of the cold pool from the previous time step, and tracking of the smaller ones are terminated. For splitting cold pools, the largest cold pool after the split is considered to be a continuation and the smaller ones are labeled as newly formed.

Through this tagging, we keep track of the history of cold pools and define *isolated* cold pools as ones that do not merge with nor split from others during their entire lifetime. We define *intersecting* cold pools as ones that merge with others during their lifetime, regardless of whether any splitting occurs. By combining the history of cold pools and the two types of boundaries defined in section 3.3, it is possible to identify regular outflow boundaries from isolated cold pools (simply called "isolated boundaries," gray shading in Figures 4f and 5c) and intersecting outflow boundaries from merging cold pools (simply called "intersecting boundaries," magenta shading in Figures 4f and 5c). We compare the characteristics of the boundaries between isolated and intersecting cold pools (section 4) and the convective clouds they trigger to gain some insight into how they organize convection in this environment (section 5). Since a large number of tracked cold pools are available as a result of the large model domain and long-term simulation, we have the liberty of choosing which cold pools to analyze. Cold pools that exist less than 30 min (three model output time steps) and those that touch the domain boundary during their lifetime are excluded from the analysis. After filtering the data this way, we are left with 16,322 isolated and 10,212 intersecting cold pools.

Examination of the time series of simulated cold pool characteristics reveals that the number of both isolated and intersecting cold pools increases with time by 21% and 67%, respectively, from the suppressed (1–10 November) to relatively active phases (11–20 November) of the MJO during our simulation. However, the mean characteristics, such as lifetime, size, depth, and intensity, of the cold pools between the two phases vary by less than 10% for isolated cold pools and less than 18% for intersecting cold pools. This suggests that the temporal variance of cold pool characteristics is relatively small. Therefore, all cold pools throughout the duration of the simulation are analyzed in this study without further separating between the suppressed and relatively active phases of the MJO.

4. Characteristics of Simulated Cold Pools

Before explaining the mechanisms of triggering and organizing convection, it is useful to investigate the physical characteristics of cold pools in this tropical warm oceanic environment. The high-resolution WRF simulation performed in this study compares reasonably well with observations of near-surface cold pool properties (Figure 3). We can use the simulation to extend the point observations and examine the spatial structure of the cold pools and their impact on the boundary layer.

Figure 6 shows the evolution of composite cold pool properties grouped by their lifetime. For simplicity, only the isolated cold pools are used in this composite. Intersecting cold pools, which could merge with others during any stage of their life cycle, introduce sporadic variations to these properties that may obscure the natural behavior of cold pools. This figure shows that cold pool properties are closely related to

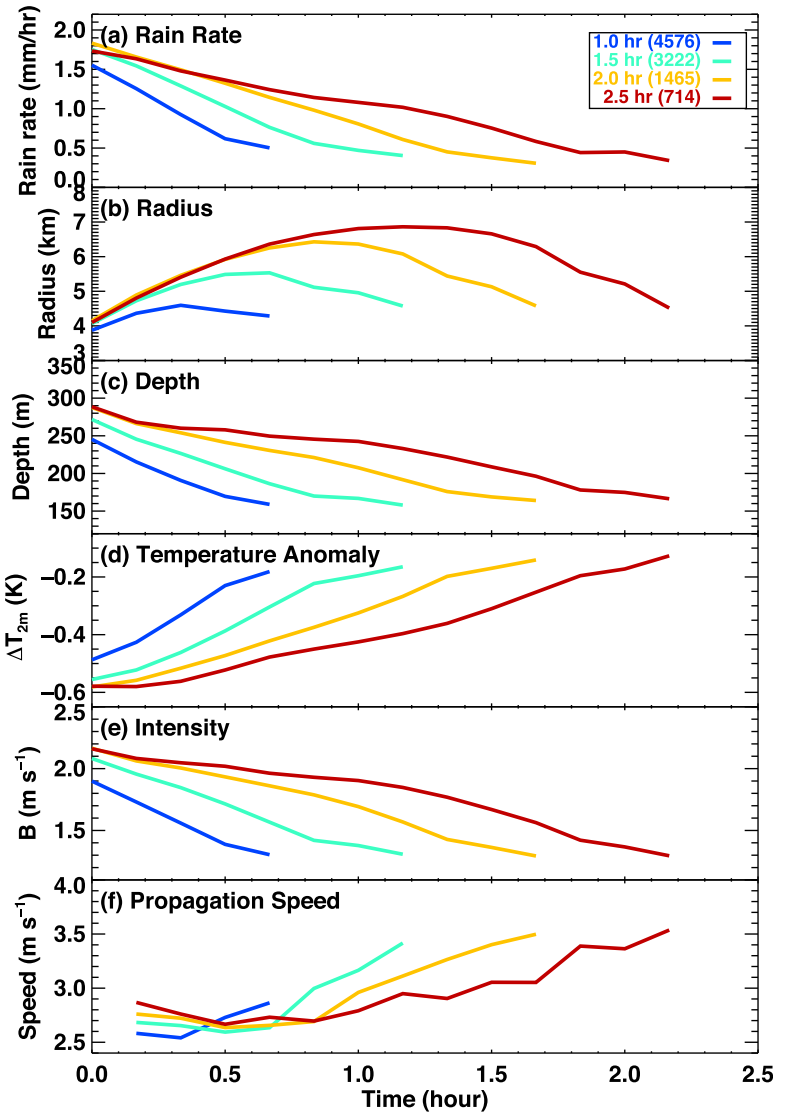

Figure 6. Composite evolution of (a) parent convection rain rate, cold pool (b) equivalent radius, (c) depth, (d) 2 m temperature anomaly, (e) intensity (vertically integrated buoyancy), and (f) advection speed. Each line represents the average of all the isolated cold pools with lifetimes that fall within the half hour bin. The number of cold pools for each lifetime bin is given in the legend.

the precipitation rate from the parent convection. Heavier or more persistent rainfall systematically produces longer lasting, larger, deeper, colder, and more intense cold pools. The maximum area (in km^2) of a cold pool appears to have a power-law relationship with the maximum rain rate (in mm hr^{-1}) of the parent convection (not shown), which can be approximated as $Area_{coldpool} = Rainrate^{0.27}$, although this relationship may be specific to the Indian Ocean during the transitioning phase of the MJO. The radius of cold pools maximizes just over halfway through their lifetime and decreases afterward. This is possibly due to the recovery of cold pools from surface fluxes and entrainment of boundary layer air above the cold pool. When the negatively buoyant air from downdrafts is not enough to balance the recovery of temperature and moisture at later stage of cold pools, part of the cold pool may no longer be negatively buoyant compared to the ambient environment. Therefore, the size of cold pools decreases until they can no longer be tracked. This is consistent with the findings of *Tompkins* [2001, see Figure 9].

The advection speed (relative to the background wind) is calculated by estimating the changes of the location of the cold pool centroid in each 10 min frame. Isolated cold pools are advected at an average speed of 2–3 m s^{-1} during their growth stage (i.e., when they are increasing in size). This is consistent with the relatively weak background wind (~1 m s^{-1}) in the boundary layer (0–2 km) during the simulation period. The

increase in advection speed during their decaying stage (i.e., when they are decreasing in size) is possibly due to dissipating cold pools losing their coherent spatial structure, resulting in more erratic changes in their centroid positions as they mix with the environment.

Previous studies suggest that the edges of cold pools are associated with enhanced moisture and recovering near-surface temperatures (i.e., less cold) due to mixing and surface fluxes, resulting in more unstable environment that favors triggering of new convection [*Tompkins*, 2001]. As discussed in section 3.3, we use near-surface negative and positive water vapor anomalies (with respect to 100 km × 100 km mean background value) to define the center and edges of cold pools, respectively. Figure 7 shows the PDF of several thermodynamic parameters averaged over the center and edges of cold pools. As in Figure 6, only the isolated cold pools are used to construct these PDFs. The results are similar for intersecting cold pools. For each tracked cold pool, we record the maximum or minimum value of each thermodynamic parameter during the lifetime of the cold pools.

With the exception of temperature and CIN, which have longer tails, the shapes of the distribution for most of these parameters are similar for the center and edges of the cold pools. However, the environment at the edge of cold pools is clearly more favorable for new convection. In contrast to the cold pool centers, the temperature depressions along the edges are mostly less than −1°C. Moist static energy is on average 1600 J kg^{-1} higher along the edges. The latent heat fluxes at the edge are on average 14% lower than those in the center. This may be because near-surface wind speeds are similar (not shown), but saturation deficits are lower along the edges, which would limit surface evaporation. CAPE is clearly higher (on average 1400 J kg^{-1} or ∼22% larger) and CIN is lower (3.7 J kg^{-1} or ∼106% smaller) along cold pool edges compared to the center. The lifted condensation level (LCL) has a fairly narrow distribution (standard deviation of 70 m) over this warm oceanic environment, but is on average 100 m (25%) lower on the edges compared to the center. These results are consistent with previous findings and suggest that using a relatively simple metric

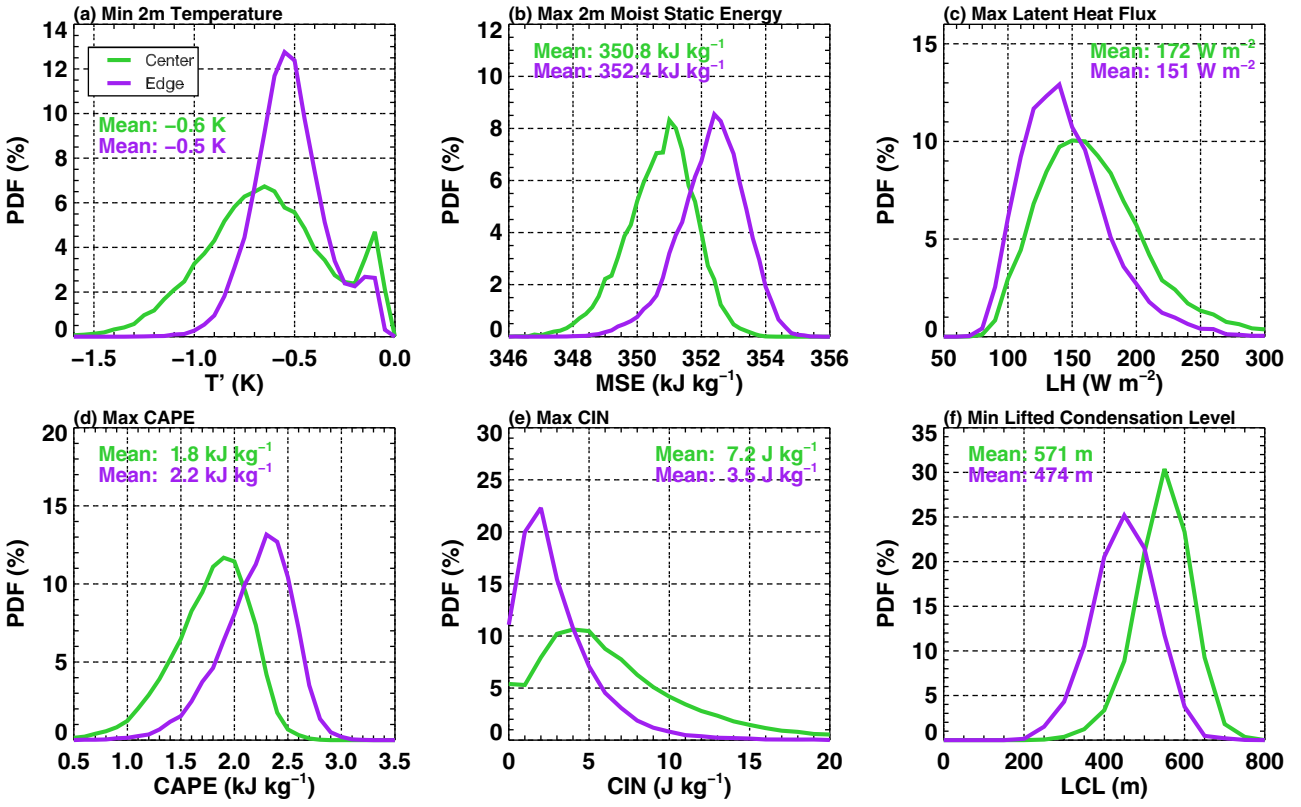

Figure 7. PDF of (a) 2 m temperature anomaly, (b) moist static energy, (c) latent heat flux, (d) convective available potential energy (CAPE), (e) convective inhibition (CIN), (f) lifted condensation level (LCL) averaged in the center (green) and edge (purple) of isolated cold pools. See text for definition of cold pool center and edge.

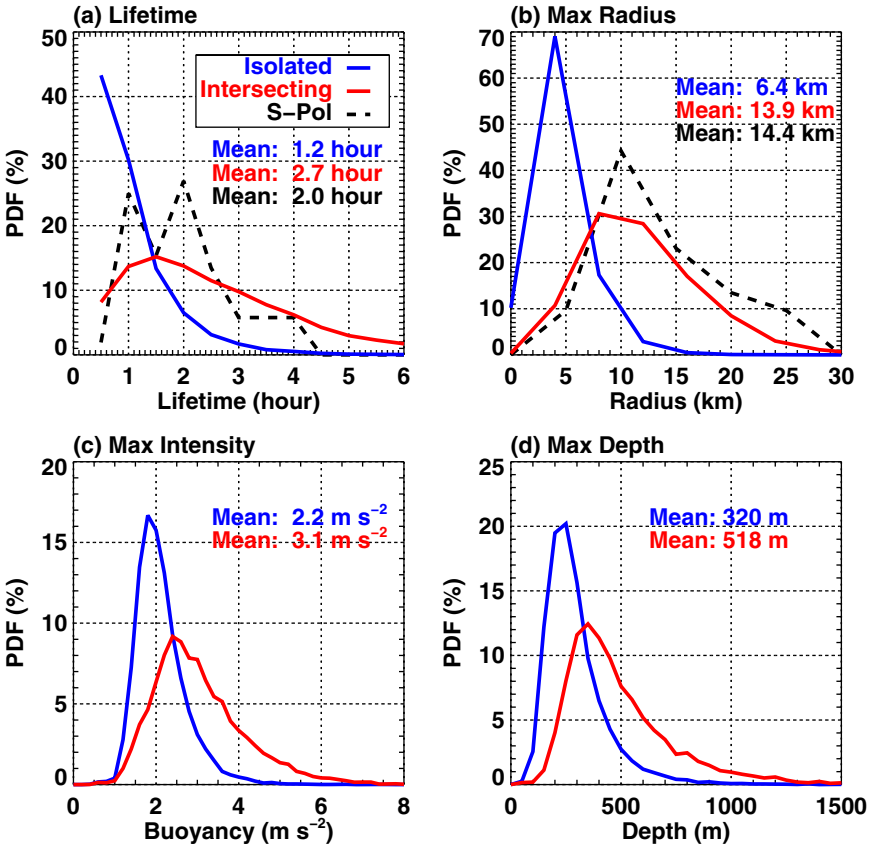

Figure 8. PDF of simulated cold pool (a) lifetime, (b) maximum equivalent radius, (c) maximum intensity, and (d) maximum depth of isolated (blue) and intersecting (red) cold pools. Intensity and depth are averaged in the entire cold pool area; maximum radius, intensity, and depth are then taken over the lifetime of each cold pool. Mean values are given in each plot. Black dash lines in Figures 8a and 8b are from S-PolKa observations, which do not separate isolated and intersecting cold pools.

(near-surface water vapor anomaly) is sufficient for identifying regions of the cold pool that are conducive to the formation of new convection.

Comparing the characteristics of isolated and intersecting cold pools reveals some striking differences (Figure 8). Intersecting cold pools last more than twice as long on average than isolated cold pools (2.7 h compared to 1.2 h). Some intersecting cold pools last longer than 6 h. When intersecting cold pools merge, they naturally become larger and the results show that their average equivalent radius is 13.9 km, or ~2.2 times as large as isolated ones (6.4 km). The PDFs of lifetime and maximum radius of cold pools observed by S-PolKa are also shown in Figures 8a and 8b. Due to the relatively small sample size (N = 52) and complex nature of intersecting cold pools in the observations, the S-PolKa-observed cold pools are not separated into isolated and intersecting categories (section 2.1). The two peaks in the lifetime (at roughly 1 and 2 h) may represent the modes associated with isolated and intersecting cold pools, or it could be affected by fast-evolving cold pools that are not well captured by the S-PolKa 15 min data. The observed PDF of maximum radius is very similar to the simulated intersecting cold pools, with an average value of 14.4 km. These comparison with observed cold pool lifetime and maximum size along with their thermodynamic properties (Figure 3) suggests that the simulation is capturing the physical characteristics of the cold pools reasonably well.

Compared to isolated cold pools, the intersecting cold pools are also 41% more intense (measured by *B*, equation (3)) and 62% deeper. This may be due to more active parent convection associated with higher rain rates and colder downdrafts. In a large portion of the isolated cold pools, the depth of the cold pool is less than the corresponding LCL height (Figure 7f). The mode depth for intersecting cold pools is comparable to the LCL height. This suggests that when the environmental air is lifted by intersecting cold pools,

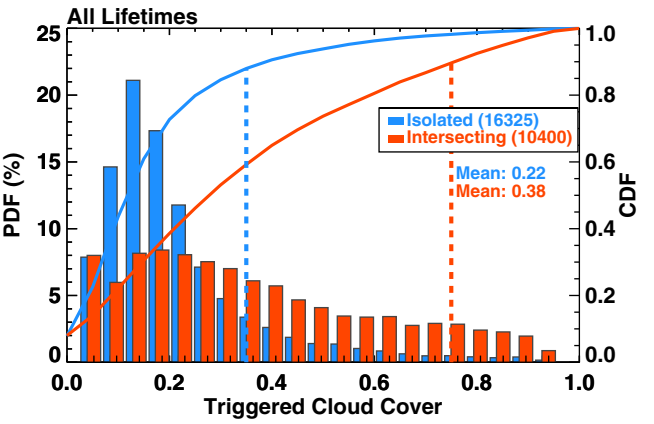

Figure 9. PDF (bars) of triggered cloud cover (cloudy area/cold pool boundary area) for regular (blue) and intersecting (orange) cold pool boundaries, cumulative density function is also plotted in solid lines, with 90th percentile cloud cover value shown in dash lines. The numbers of cold pool sample and mean cloud cover are shown in the legend.

there is a higher probability of reaching the LCL and forming new clouds compared to isolated cold pools. This finding is further examined in the next section.

5. Organization of Convection by Cold Pools

5.1. Triggering of Convection by Cold Pools

Since the locations and boundaries of the cold pools are tracked in time, the clouds formed by isolated and intersecting cold pools can be recorded. Column LWP, not including rain, from the simulated cloud condensate (e.g., Figures 4 and 5) is used to identify convective clouds triggered by the cold pools. A column is defined as cloudy if LWP > 10 g m^{-2}. We choose a low LWP threshold to include most of the cumulus clouds that may be triggered by cold pools. LWP < 100 g m^2 is considered "thin liquid clouds" [*Turner et al.*, 2007]. The triggered cloud cover along the cold pool boundaries is then calculated as the ratio between the number of cloudy pixels and the total number of pixels that the cold pool boundary encompasses (e.g., Figure 4f). A triggered cloud cover ratio of one means that the entire area of the cold pool boundary is cloudy. Since intersecting cold pools are significantly larger than isolated ones (Figure 8b), it is expected that their outflow boundary areas (and consequently the amount of triggered clouds) will also be larger. We minimize this dependency by considering cloud cover ratios. This metric is equivalent to the clouds per unit area along the cold pool boundary.

Figure 9 shows the PDFs of triggered cloud cover by isolated and intersecting cold pool boundaries. Since cold pools can trigger convective clouds during any stage of their lifetime, the maximum triggered cloud cover in the boundary region is used for each of the tracked cold pools. The results show that, on average, triggered cloud cover by intersecting boundaries (0.38) is 73% higher than for clouds triggered by isolated boundaries (0.22). While the shape of the distribution is similar for isolated and intersecting cold pools, the distribution for intersecting boundaries has a longer tail toward higher cloud cover. This is also evident in the cumulative density function (solid lines in Figure 9). The 90th percentile of cloud cover value (marked by dashed lines in Figure 9) is 0.75 for intersecting boundaries and 0.35 for isolated boundaries. This result shows quantitatively that intersecting cold pools are more efficient at triggering convective clouds compared to isolated cold pools. This is qualitatively consistent with the S-PolKa radar observations (section 2).

In order to understand the mechanisms for the enhanced ability of intersecting cold pool to trigger convection, several thermodynamic parameters for isolated and intersecting cold pool boundaries are compared. Table 2 shows the mean values averaged over all isolated and intersecting cold pool boundaries and the difference between the two. We only focus on the mean value since the shapes of their PDFs (which are in general Gaussian) are similar (not shown). Most of the thermodynamic parameters are comparable between the isolated and intersecting boundaries. There is no difference in near-surface moist static energy and CAPE. Intersecting boundaries have a 17% higher water vapor anomaly, but also have higher CIN. These

Table 2. Average Values of Thermodynamic Parameters for Isolated and Intersecting Cold Pool Boundaries[a]

	B (m s^{-1})	q'_v (g kg^{-1})	*MSE* (KJ kg^{-1})	*LH* (W m^{-2})	*SH* (W m^{-2})	*CAPE* (KJ kg^{-1})	*CIN* (J kg^{-1})	*LCL* (m)	*LFC* (m)
Isolated boundary	2.0	0.47	354	130	12	2.4	1.5	504	553
Intersecting boundary	2.7	0.55	354	145	17	2.4	3.2	453	534
Difference (%)	35%	17%	0%	12%	42%	0%	113%	−10%	−3%

[a]*B*: cold pool intensity as in equation (3), q'_v: 2 m water vapor anomaly, *MSE*: 2 m moist static energy, *LH*: surface latent heat flux, *SH*: surface sensible heat flux, *CAPE*: convective available potential energy, *CIN*: convective inhibition, *LCL*: lifted condensation level, *LFC*: level of free convection, and Relative differences are computed by (Intersecting – Isolated)/Isolated.

results suggest that the thermodynamic conditions within the intersecting boundaries are not significantly more favorable for convection compared to isolated boundaries. Since thermodynamics alone cannot explain the differences in the amount of triggered convective clouds, our attention is turned to the dynamics.

We showed that the buoyancy-defined and water vapor anomaly-defined cold pool boundaries are collocated with enhanced updrafts along the outflow boundaries (Figures 4 and 5), thus the secondary updrafts induced by cold pool outflows can be quantified within the boundary regions. Figure 10 shows the secondary updraft profiles for both isolated and intersecting cold pool boundaries. Updraft velocities (defined as $w > 0.1$ m s^{-1}) along the cold pool boundaries are averaged at each height and time that a cold pool is identified. The maximum value at each height during the lifetime of each cold pool is selected. This generates one profile of maximum updraft velocity for each cold pool. We then construct a distribution of updraft velocities using the ensemble of cold pools. Further, only a subset of cold pools with similar lifetime (2–2.5 h) are included in Figure 10. The results shown in Figure 10 are consistent across all lifetimes and differ only in magnitude. We show results from ~2 h lifetimes because of the relatively comparable number of samples between isolated and intersecting cold pools.

The median values of the subcloud layer secondary updrafts for isolated and intersecting cold pools are similar at all heights, meaning that many of the weak updrafts of isolated and intersecting boundaries are similar. The differences appear mostly in the tails of the distribution (higher percentiles) and with increasing height. This suggests that the dynamical differences between isolated and intersecting cold pools are primarily in the frequency of stronger updrafts, which are more important for triggering new convection. For example, at the mean LCL/LFC height, the 75th–99th percentile of secondary updrafts induced by intersecting cold pools are 12–45% faster than that of isolated cold pools. For a given intersecting cold pool, the secondary updrafts along the portion of the boundary that collides with adjacent cold pool are 10–25% faster than those along the noncolliding boundaries. This suggests that while some of the differences in Figure 10 can be attributed to intersecting cold pools being inherently more intense (perhaps resulting from stronger downdrafts) than isolated cold pools, the collision of outflow boundaries does enhance the speed of the secondary updraft. Somewhat unexpectedly, the lower 25th percentile of updraft velocities for intersecting cold pools is slightly lower than for isolated cold pools. This may be caused by merging cold pools that are initially in close proximity, such that their intersecting boundaries do not have enough time to accelerate to enhance the secondary updrafts. We also note that the median to upper quartile secondary updraft values induced by cold pools near the LCL/LFC are similar to those used by *Rio et al.* [2013] in their parameterized cold pool induced subcloud lifting scheme over tropical oceans.

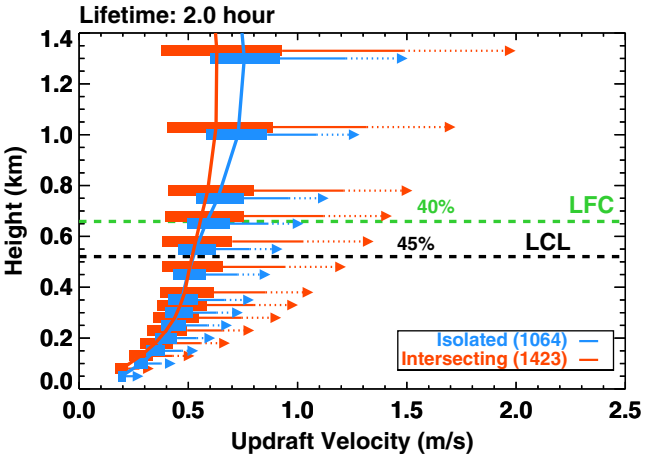

Figure 10. Box whisker plot of updraft velocity profiles averaged at the boundaries of isolated (blue) and intersecting (orange) cold pools lasting between 2 and 2.5 h. They are displaced slightly in the vertical for clarity. Solid line profiles are median values, boxes are 25th and 75th percentiles, horizontal solid lines are 95th percentiles, and triangles are 99th percentiles. Mean lifted condensation level (LCL, black dash) and level of free convection (LFC, green dash) are also shown. The numbers on the LCL/LFC heights are 99th percentile updraft velocity (w) relative differences $[(w_{intersecting} - w_{isolated})/w_{isolated}]$ between intersecting and isolated cold pools at those heights, respectively. Number of cold pool samples is shown in the legend.

These results show that intersecting cold pools are more likely to create stronger secondary updrafts (> 1 m s^{-1}) that favor triggering of new convection. Faster updrafts explain why intersecting cold pools trigger 72% more convective clouds on average than isolated cold pools (Figure 9). Stronger outflows and the collisions from intersecting cold pools enhance the strength of the secondary updrafts. These stronger updrafts are

more likely to lift the environmental air above the negatively buoyant cold pool outflow and trigger more convective clouds.

The dynamical convective triggering mechanism in our results is independent of the thermodynamic mechanism proposed by *Tompkins* [2001], which focused specifically on isolated cold pools where clouds developed after the temperature depression from cold pool recovers. It is possible that such a mechanism is also in play in this study: the environment is more convectively favorable at the edge of the cold pools (Figure 7) for both isolated and intersecting cold pools (Figure 7). However, we find the difference between isolated and intersecting cold pools lies in the dynamics, and we are able to quantify the differences in the magnitude of secondary updrafts and their contribution to the triggering of convective clouds in a warm oceanic environment.

5.2. Organization of Deep Convection by Cold Pools

In this subsection, the fate of the triggered convection along cold pool outflow boundaries is investigated to further investigate the mechanisms responsible for the development of deep convection. The maximum convective cloud-top heights triggered by isolated and intersecting cold pools are shown as functions of secondary updraft velocity at the LCL and triggered cloud size (equivalent radius $r_e = \sqrt{A/\pi}$) in Figure 11. The area of all contiguous cloudy pixels (LWP $>$ 10 g kg^{-1}) in the outflow boundary region is A. Cloud-top height is computed using the total condensate mixing ratio q_{total} (the sum of cloud, rain, graupel, snow, and ice mixing ratios). If q_{total} in a grid point is larger than 10^{-3} g kg^{-1} it is considered cloudy. Secondary updraft velocity is the same as that described in the previous subsection. We use the maximum secondary updraft, cloud equivalent radius, and cloud-top height for each tracked cold pool to construct the statistics.

Figure 11 shows that clouds triggered by intersecting cold pools are on average deeper than those by isolated cold pools. Surprisingly, cloud-top height appears to be more sensitive to the triggered cloud radius than the strength of the secondary updraft near the cloud base. That is, the deepest clouds (cloud-top height $>$ 10 km) most frequently occur only along intersecting cold pool boundaries when the triggered cloud radius is above 5 km. This result implies that differences in cloud-top height between isolated and intersecting cold pools are primarily due to the fact that larger clouds triggered at the intersecting cold pool boundaries are subject to reduced entrainment of subsaturated environmental air which allows them to develop into deeper convection. This is consistent with the "near environment" hypothesis proposed by *Böing et al.* [2012], where they found deeper clouds developed from wider cloud bases. *Schlemmer and Hohenegger* [2014] further support this hypothesis through a series of cloud-resolving model simulations for a variety of atmospheric conditions over land and ocean. They

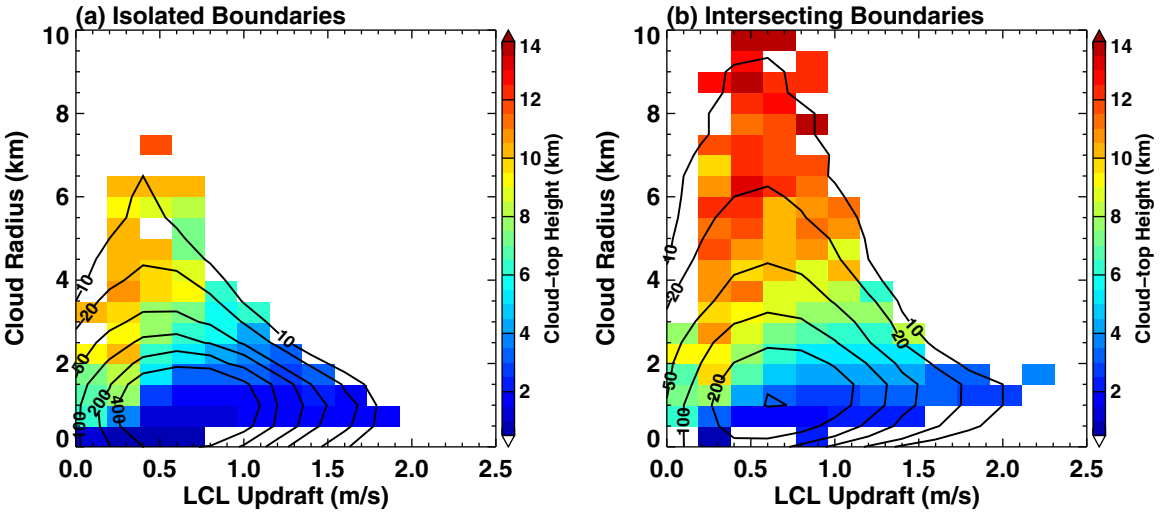

Figure 11. Mean triggered convective cloud-top heights (shaded) as functions of mean updraft velocity at lifted condensation level (LCL) and triggered cloud equivalent radius in (a) isolated cold pool boundaries, and (b) intersecting cold pool boundaries. Contours show the number of samples.

reported that larger moist patches formed outside of evolving cold pools, supporting larger convective cloud clusters to form over them. These larger clouds are less affected by entrainment and eventually become deeper.

While the difference in cloud-top height may arise from the increased cloud density associated with intersecting cold pools, it could also result from differences in the large-scale environment. Our simulation covers the transition period from the suppressed (1–10 November) to active (11–20 November) phases of the MJO. This transition is generally associated with increasing convective activity and moistening of the mid-troposphere [*Johnson and Ciesielski*, 2013; *Powell and Houze*, 2013], characterized by the weakening of equatorward midlevel advection of dry air as the Rossby gyres from the preceeding MJO episode recede eastward and low-level convergence and associated uplift increase [Figure 17 and Figure 22 in *Johnson and Ciesielski*, 2013]. These two processes work in concert to accelerate the rapid shallow-to-deep transition that marks the initiation of MJO as shown by high-resolution model simulations [*Hagos et al*., 2014a]. Given these large-scale conditions, one might expect that in a dry environment precipitating convection and the cold pools it produces may be more isolated and less likely to interact. Conversely, extensive convection present in a moist environment may produce more numerous cold pools that increase the chances of collision. As a result, frequent triggering and continued development of new convection may be dependent on the large-scale environmental moisture rather than the effect of intersecting cold pools.

To test the sensitivity to the large-scale environmental moisture, the dependence of cloud-top height on large-scale precipitable water (PW), triggered cloud radius, and spacing among clouds is shown in Figure 12. Large-scale PW is computed by averaging the column integrated water vapor in a 100 km $\times$ 100 km area centered on each cold pool. The equivalent spacing (S_e in km) among clouds is defined as:

$$S_e = \frac{1}{N}\sum(d_{centroid} - r_{e1} - r_{e2}) \tag{4}$$

where N is the number of cloud clusters in the cold pool boundary region, $d_{centroid}$ is the distance between the centroids of the two closest cloud clusters, and r_{e1}, r_{e2} are the equivalent radii of the closest cloud clusters. Assuming two of the closest clouds have circular shapes, the quantity in the parenthesis in equation (4) corresponds to the distance between the edges of the circular clouds. For a closely spaced pair of elongated clouds, the equivalent spacing can become negative if $(r_{e1}+r_{e2}) > d_{centroid}$. By averaging all of the closest edge distances among clouds over the cold pool boundary region, S_e represents a measure of the "gaps" between clouds. The smaller the S_e, the closer the clouds are to each other which can minimize the entrainment of subsaturated environmental air.

To the first-order, convective cloud-top heights vary with large-scale PW in a nonlinear fashion [see *Del Genio et al*., 2012; their Figure 4]. Most triggered convective cloud tops are below 6 km when large-scale PW is less than 4.8 cm (dashed line in Figure 12). They often become deeper than 8 km as large-scale PW approaches 5.5 cm. However, for the same moisture conditions, convective cloud tops reaching 8 km and above occur more frequently for clouds with larger area and less equivalent spacing. The different distributions of the size and clustering of clouds accounts for the difference in cloud-top heights over the intersecting and isolated cold pool boundaries. The relative humidity profiles for a given large-scale PW value shows that the average humidity in the subcloud layer is almost identical between the isolated and intersecting cold pool boundaries. In the low-to-mid troposphere, relative humidity differs by only a few percent (not shown). This suggests that the vertical structure of large-scale humidity is similar. Therefore, given similar environment moisture profiles, larger clouds and smaller spacing between clouds over intersecting cold pool boundaries favor development of deep convection.

The role of intersecting cold pools in the organization of deep convection is primarily twofold: (1) the triggering of more clouds along the cold pool boundary is possibly due to more frequent stronger secondary updrafts, and (2) forcing the triggered convective clouds closer to each other and forming larger cloud clusters that reduce the drying effect of entrainment, and allow development of the triggered convective clouds into deep convection. The importance of intersecting cold pools to organized deep

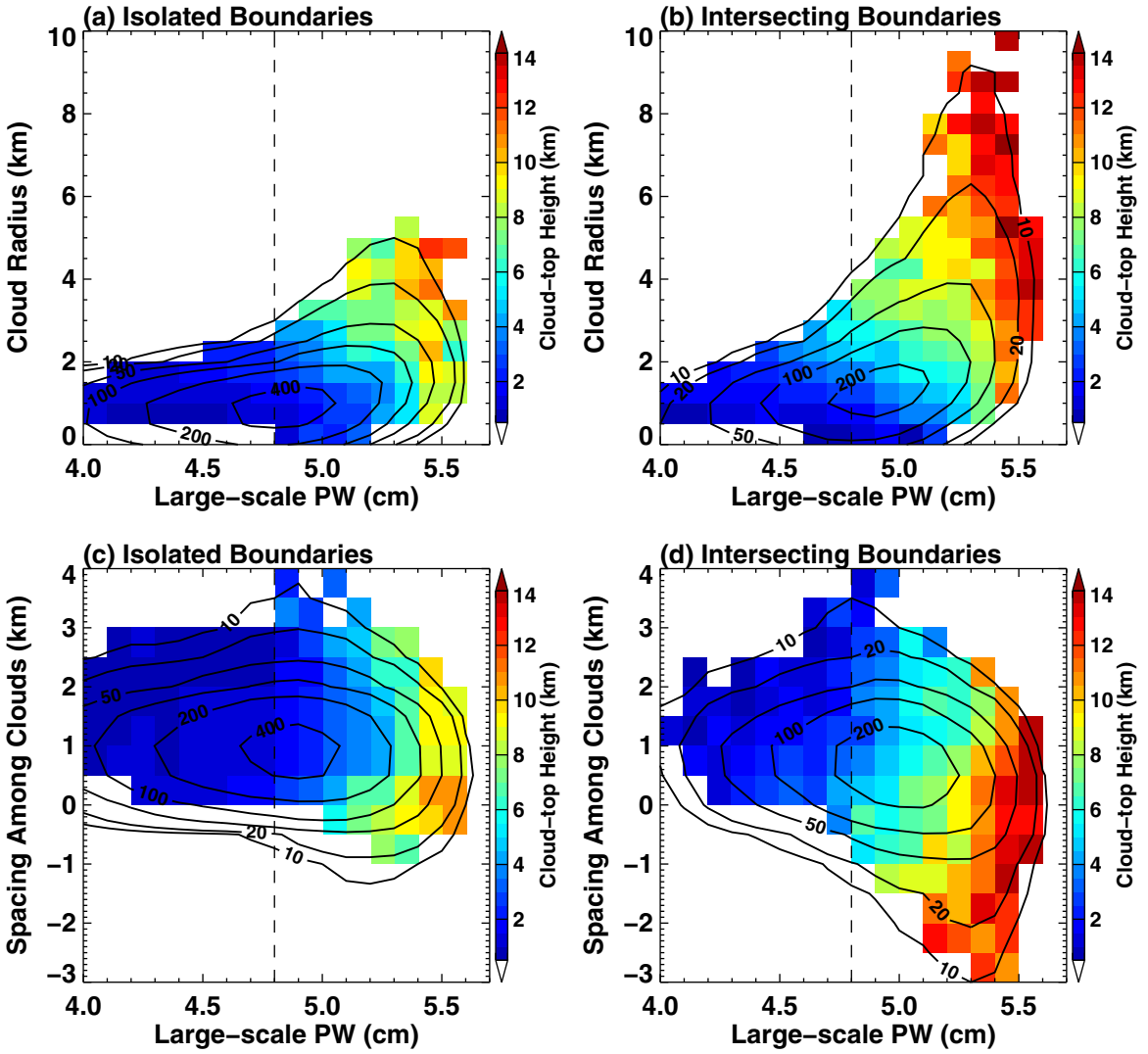

Figure 12. Same as Figure 11 except for large-scale precipitable water (PW), (a,b) triggered cloud equivalent radius, (c,d) equivalent spacing among clouds. Dash line indicates large-scale PW needed for deeper clouds to occur. See text for details about equivalent spacing among clouds.

convection also implies that the density of cold pools, which strongly influences subsequent convective cloud aggregation, is an important parameter as well. For example, in the cold pool parameterization developed by *Grandpeix and Lafore* [2010], the density of cold pools is prescribed. Results from this study suggest that the density of cold pools and the associated secondary deep convection depend on the large-scale environment and preexisting convective activity, and should be parameterized based on metrics such as precipitable water content and downdraft intensity.

6. Summary and Conclusions

We examine the mechanisms of convective cloud organization by cold pools in a warm tropical oceanic environment. During the 2011 AMIE/DYNAMO field campaign, the S-PolKa radar deployed on the Addu Atoll, Maldives, and the *R/V Revelle* stationed in the equatorial Indian Ocean frequently observed cold pools produced by precipitating convection over the warm equatorial Indian Ocean.

The S-PolKa radar's high sensitivity allowed for precipitating and nonprecipitating echoes to be observed. During the suppressed phases of the MJO, when cold pools are more easily identified, the

maximum spatial extent and duration of cold pools are obtained by manually tracking them using the S-PolKa surveillance scans. Cold pools produced by nearby convection were commonly observed to intersect, either serving as a focal point for new convective initiation or merging to form larger cold pools. Passages of cold pools create distinct thermodynamic changes in the near-surface layer that can be detected in the time series of air temperature observations. We find that the observed cold pools on average cool the near-surface air by 1.4°C, increase the water vapor mixing ratio by 0.1 g kg^{-1}, and the wind speed by 2.4 m s^{-1}, and generate a 22 W m^{-2} enhancement of the surface latent heat flux over the ocean (Figure 3).

A high-resolution (500 m horizontal grid spacing) simulation using the WRF model over a large region (1000 km × 500 km, Figure 2) is performed during the transition from the suppressed to active phases of the November MJO episode during AMIE/DYNAMO (1–20 November 2011). The model is able to simulate the lifetime, maximum spatial extent, and thermodynamic properties of cold pools that are comparable to the S-PolKa radar and *R/V Revelle* observations.

From the WRF simulation, we identify individual cold pools using a watershed technique and quantify their size and spatial characteristics. The simulated cold pools are tracked in time using an automated tracking algorithm and two distinct types of cold pools, isolated and intersecting, are identified. Combining the history of cold pools with their spatial structures, the boundaries of isolated and intersecting cold pools and the convective clouds developed along their edges are identified. The characteristics of these two types of cold pools, their thermodynamic and dynamic structures, and the convective clouds triggered at their boundaries are compared.

More persistent rainfall systematically produces longer lasting, larger, deeper, and colder cold pools (Figure 6). The maximum area of cold pools has a power-law relationship with the maximum rain rate of the parent convection ($Area_{coldpool} = Rainrate^{0.27}$). The environment at the edge of cold pools, which is characterized by higher moist static energy, higher convective available potential energy (CAPE), lower convective inhibition (CIN), and a lower lifted condensation level (LCL), is more favorable for new convection to form. Compared to isolated cold pools, intersecting cold pools last on average more than twice as long, grow to ~2.2 times as large, are 41% more intense (measured by buoyancy), and are 62% deeper. On average, the intersecting cold pools trigger 73% more convective cloud cover compared to isolated cold pools. This is mainly due to the stronger colliding outflows from intersecting cold pools. The averaged secondary updraft velocities at LCL height along the intersecting cold pool boundaries are up to 45% faster.

The fate of the triggered convection along the cold pool outflow boundary is investigated by comparing the maximum cloud-top height of convection triggered by isolated and intersecting cold pools in similar large-scale moisture environments. In a dry environment (large-scale precipitable water < 4.8 cm), neither isolated nor intersecting cold pools are sufficient to trigger deep convection. Surprisingly in a moist environment (large-scale precipitable water > 4.8 cm), deep convection develops more often from larger cloud clusters and smaller spacing among them over the intersecting cold pool boundaries, rather than from stronger secondary updrafts near-cloud base. This finding is in agreement with the "near environment" hypothesis proposed in previous studies [e.g., *Böing et al.* 2012; *Schlemmer and Hohenegger* 2014]. The mechanisms of convective cloud organization by cold pools in a moist oceanic environment can be summarized in the schematic depicted in Figure 13 as follows:

1. For isolated cold pools, precipitation-driven downdrafts push the moist environment air in the boundary layer outward after contacting the surface. Cold pools lift the relatively moist environmental air from the boundary layer and can create new convective clouds along the cold pool boundary. Continued development of these convective clouds is often limited by the entrainment of dry environmental air above the boundary layer when their size is small and the spacing is large between them.
2. For intersecting cold pools, more convective clouds are triggered by stronger outflow boundaries. At the intersecting boundary, when more convective clouds are generated in closer proximity to each other, the spacing among them is reduced and larger clouds and cloud clusters are more

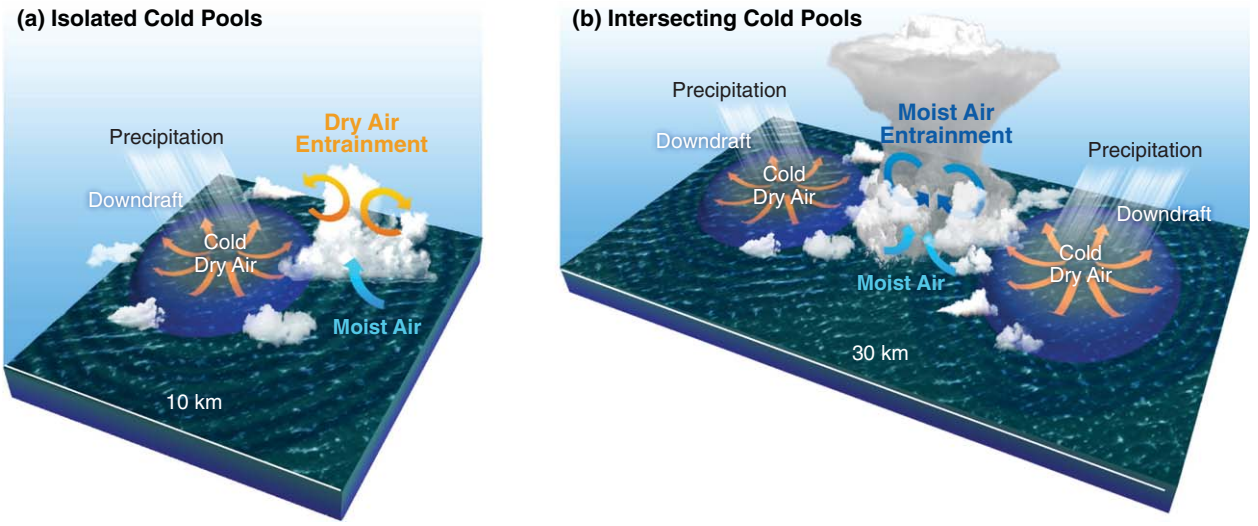

Figure 13. Schematic of the mechanism of convective organization by cold pools. For isolated cold pools (a), moist air at cold pool edges are lifted up by the downdraft-induced outflow and trigger new convective clouds, but entrainment of relatively drier environment air above the boundary layer oftentimes limit the vertical growth. For intersecting cold pools (b), more clouds are triggered at their intersecting boundaries and the distance between clouds is reduced, creating larger cloud clusters. As a result, entrainment is limited within the nearby moist cloudy air, favoring the growth of the new clouds into deep convection.

commonly formed. These larger clouds are then subject to reduced entrainment of dry environmental air above the boundary layer, which then have higher probability of further developing into deep convection.

The dependence of convective cloud entrainment rates on the cold pools that trigger them has important implications for the design of convective parameterizations. Previous studies have shown that entrainment rate varies with height [*Lin and Arakawa*, 1997] and with thermodynamic variables such as CAPE and CIN [*Cohen*, 2000], relative humidity [*Bechtold et al*., 2008], and buoyancy [*Chikira and Sugiyama*, 2010]. We find that the entrainment of dry air is also related to the cloud spacing. This spacing is driven by cold pool dynamics because new clouds tend to form on the edges of isolated cold pools and aggregate at the colliding boundaries of intersecting cold pools. The distribution of the spacing among the clouds and hence the overall entrainment rate is likely sensitive to the strength of the downdrafts that control the subsequent shallow clouds. One way to parameterize this effect is to incorporate the effect of downdrafts and cold pool dynamics on the statistical properties of the entrainment rate, such that larger rain rates lead to an increased probability of reduced spacing among clouds. As a result, the clouds could "shield" each other from the entrainment of dry air, effectively reducing the entrainment rate and allowing continued growth of the triggered shallow clouds into deep convection.

A first step in parameterization of the cold pool effects is recognizing that boundary layer clouds are not randomly distributed. Instead a large number of clouds are typically aggregated on the order of tens of kilometers around otherwise clear and dry environments. Thus the probability of a cloud taking advantage of the aggregation to grow into deep convection would be larger than compared to if the populations of shallow clouds were randomly distributed. Therefore, a portion of a GCM grid box within the PBL needs to be partitioned into such regions. The sensitivity of the size and lifetime of the aggregations to grid-scale environmental variables can be derived from mass and energy conservation arguments [*Park*, 2014] and density current dynamics [*Grandpeix and Lafore*, 2010]. The potential for secondary convection depends on the intensity of the downdrafts that generates the cold pools and the mixing processes, which in turn are controlled by cold pool area and depth through gravity wave mass adjustment. For example, strong cold pools have been shown to force uplift and deep convection almost adiabatically with little entrainment of dry surrounding air [*Piriou et al*., 2007]. High-resolution model simulations like the one conducted in this study begin to untangle the complex relationships between cold pools and convection and help constrain key parameters on which they depend.

Acknowledgment
The DYNAMO field campaign data used in this paper is available at NCAR's Earth Observing Laboratory's DYNAMO Data Catalogue https://www.eol.ucar.edu/field_projects/dynamo. The data set names are: R/V Roger Revelle Flux, Near-Surface Meteorology, and Navigation Data and S-PolKa Radar, fully corrected, merged, final moments data in cfRadial format. This research is based on work supported by the Biological and Environmental Research of the U.S. Department of Energy (DOE) Office of Science as part of the Atmospheric System Research Program and the Regional and Global Climate Modeling Program. The author at the University of Washington is supported by NSF grant AGS-1355567 and DOE ASR grant DE-SC0008452. Computing resources for the simulations are provided by the Oak Ridge Leadership Computing Facility (OLCF) and the National Energy Research Scientific Computing Center (NERSC). The Pacific Northwest National Laboratory is operated for DOE by Battelle Memorial Institute under contract DE-AC05-76RL01830.

References

Bechtold, P., M. Köhler, T. Jung, F. Doblas-Reyes, M. Leutbecher, M. J. Rodwell, F. Vitart, and G. Balsamo (2008), Advances in simulating atmospheric variability with the ECMWF model: From synoptic to decadal time-scales, *Q. J. R. Meteorol. Soc.*, *134*(634), 1337–1351, doi:10.1002/qj.289.

Böing, S. J., H. J. J. Jonker, A. P. Siebesma, and W. W. Grabowski (2012), Influence of the subcloud layer on the development of a deep convective ensemble, *J. Atmos. Sci.*, *69*(9), 2682–2698, doi:10.1175/JAS-D-11-0317.1.

Bryan, G. H., and M. D. Parker (2010), Observations of a squall line and its near environment using high-frequency Rawinsonde launches during VORTEX2, *Mon. Weather Rev.*, *138*(11), 4076–4097, doi:10.1175/2010MWR3359.1.

Chikira, M., and M. Sugiyama (2010), A cumulus parameterization with state-dependent entrainment rate. Part I: Description and sensitivity to temperature and humidity profiles, *J. Atmos. Sci.*, *67*(7), 2171–2193, doi:10.1175/2010JAS3316.1.

Chuda, T., H. Niino, K. Yoneyama, M. Katsumata, T. Ushiyama, and O. Tsukamoto (2008), A statistical analysis of surface turbulent heat flux enhancements due to precipitating clouds observed in the tropical Western Pacific, *J. Meteorol. Soc. Jpn.*, *86*(3), 439–457.

Cohen, C. (2000), A quantitative investigation of entrainment and detrainment in numerically simulated cumulonimbus clouds, *J. Atmos. Sci.*, *57*(10), 1657–1674, doi:10.1175/1520-0469(2000)057<1657:AQIOEA>2.0.CO;2.

Davison, J. L., R. M. Rauber, and L. Di Girolamo (2013), A revised conceptual model of the tropical marine boundary layer. Part II: Detecting relative humidity layers using Bragg scattering from S-Band radar, *J. Atmos. Sci.*, *70*(10), 3025–3046, doi:10.1175/JAS-D-12-0322.1.

Del Genio, A. D., Y. Chen, D. Kim, and M.-S. Yao (2012), The MJO transition from shallow to deep convection in CloudSat/CALIPSO data and GISS GCM simulations, *J. Clim.*, *25*(11), 3755–3770, doi:10.1175/jcli-d-11-00384.1.

Dougherty, E. R. (1992), *An Introduction to Morphological Image Processing*, 161 pp., SPIE Opt. Eng. Press., INTERNATIONAL, Bellingham, Wash.

Droegemeier, K. K., and R. B. Wilhelmson (1985), Three-dimensional numerical modeling of convection produced by interacting thunderstorm outflows. Part I: Control simulation and low-level moisture variations, *J. Atmos. Sci.*, *42*(22), 2381–2403, doi:10.1175/1520-0469(1985)042<2381:TDNMOC>2.0.CO;2.

Dudhia, J. (1989), Numerical study of convection observed during the winter monsoon experiment using a mesoscale two-dimensional model, *J. Atmos. Sci.*, *46*(20), 3077–3107, doi:10.1175/1520-0469(1989)046<3077:NSOCOD>2.0.CO;2.

Fairall, C. W., E. F. Bradley, J. E. Hare, A. A. Grachev, and J. B. Edson (2003), Bulk parameterization of air-sea fluxes: Updates and verification for the COARE algorithm, *J. Clim.*, *16*(4), 571–591, doi:10.1175/1520-0442(2003)016<0571:BPOASF>2.0.CO;2.

Feng, Z., X. Dong, B. Xi, S. A. McFarlane, A. Kennedy, B. Lin, and P. Minnis (2012), Life cycle of midlatitude deep convective systems in a Lagrangian framework, *J. Geophys. Res.*, *117*, D23201, doi:10.1029/2012JD018362.

Feng, Z., S. A. McFarlane, C. Schumacher, S. Ellis, J. Comstock, and N. Bharadwaj (2014), Constructing a merged cloud-precipitation radar dataset for tropical convective clouds during the DYNAMO/AMIE experiment at Addu Atoll, *J. Atmos. Oceanic Technol.*, *31*(5), 1021–1042, doi:10.1175/JTECH-D-13-00132.1.

Grandpeix, J.-Y., and J.-P. Lafore (2010), A density current parameterization coupled with Emanuel's convection scheme. Part I: The models, *J. Atmos. Sci.*, *67*(4), 881–897, doi:10.1175/2009jas3044.1.

Grandpeix, J.-Y., J.-P. Lafore, and F. Cheruy (2010), A density current parameterization coupled with Emanuel's convection scheme. Part II: 1D simulations, *J. Atmos. Sci.*, *67*(4), 898–922, doi:10.1175/2009jas3045.1.

Hagos, S., Z. Feng, S. McFarlane, and L. R. Leung (2013), Environment and the lifetime of tropical deep convection in a cloud-permitting regional model simulation, *J. Atmos. Sci.*, *70*(8), 2409–2425, doi:10.1175/JAS-D-12-0260.1.

Hagos, S., Z. Feng, K. Landu, and C. N. Long (2014a), Advection, moistening, and shallow-to-deep convection transitions during the initiation and propagation of Madden-Julian Oscillation, *J. Adv. Model. Earth Syst.*, *6*, 938–949, doi:10.1002/2014MS000335.

Hagos, S., Z. Feng, C. Burleyson, K.-S. Lim, C. N. Long, D. Wu, and G. Thompson (2014b), Evaluation of high resolution simulations of cloud populations in Madden-Julian oscillation using data collected during AMIE/DYNAMO field campaign, *J. Geophys. Res. Atmos.*, *119*, 12,052–12,068, doi:10.1002/2014JD022143.

Hong, Y., K.-L. Hsu, S. Sorooshian, and X. Gao (2004), Precipitation estimation from remotely sensed imagery using an artificial neural network cloud classification system, *J. Appl. Meteorol.*, *43*(12), 1834–1853, doi:10.1175/JAM2173.1.

Hourdin, F., et al. (2013), LMDZ5B: The atmospheric component of the IPSL climate model with revisited parameterizations for clouds and convection, *Clim. Dyn.*, *40*(9-10), 2193–2222, doi:10.1007/s00382-012-1343-y.

Iacono, M. J., E. J. Mlawer, S. A. Clough, and J.-J. Morcrette (2000), Impact of an improved longwave radiation model, RRTM, on the energy budget and thermodynamic properties of the NCAR community climate model, CCM3, *J. Geophys. Res.*, *105*(D11), 14,873–14,890, doi:10.1029/2000JD900091.

Janjic, Z. I. (2002), Nonsingular implementation of the Mellor-Yamada level 2.5 scheme in the NCEP Meso model, *NCEP Off. Note 437*, 1–61.

Johnson, R. H., and P. E. Ciesielski (2013), Structure and properties of Madden-Julian oscillations deduced from DYNAMO sounding arrays, *J. Atmos. Sci.*, *70*(10), 3157–3179, doi:10.1175/JAS-D-13-065.1.

Khairoutdinov, M. F., and D. Randall (2006), High-resolution simulation of shallow-to-deep convection transition over land, *J. Atmos. Sci.*, *63*(12), 3421–3436, doi:10.1175/Jas3810.1.

Khairoutdinov, M. F., S. K. Krueger, C. H. Moeng, P. A. Bogenschutz, and D. A. Randall (2009), Large-eddy simulation of maritime deep tropical convection, *J. Adv. Model. Earth Syst.*, *1*, 15, doi:10.3894/JAMES.2009.1.15.

Krueger, S. K. (1988), Numerical simulation of tropical cumulus clouds and their interaction with the subcloud layer, *J. Atmos. Sci.*, *45*(16), 2221–2250, doi:10.1175/1520-0469(1988)045<2221:NSOTCC>2.0.CO;2.

Kuang, Z., and C. S. Bretherton (2006), A mass-flux scheme view of a high-resolution simulation of a transition from shallow to deep cumulus convection, *J. Atmos. Sci.*, *63*(7), 1895–1909, doi:10.1175/JAS3723.1.

Li, Z., P. Zuidema, and P. Zhu (2014), Simulated convective invigoration processes at trade-wind cumulus cold pool boundaries, *J. Atmos. Sci.*, *71*(8), 2823–2841, doi:10.1175/JAS-D-13-0184.1.

Lima, M. A., and J. W. Wilson (2008), Convective storm initiation in a moist tropical environment, *Mon. Weather Rev.*, *136*(6), 1847–1864, doi:10.1175/2007MWR2279.1.

Lin, C., and A. Arakawa (1997), The macroscopic entrainment processes of simulated cumulus ensemble. Part I: Entrainment sources, *J. Atmos. Sci.*, *54*(8), 1027–1043, doi:10.1175/1520-0469(1997)054<1027:TMEPOS>2.0.CO;2.

Martini, M. N., W. I. Gustafson, Q. Yang, H. Xiao (2014), Impact of resolution on simulation of closed mesoscale cellular convection identified by dynamically guided watershed segmentation, *J. Geophys. Res. Atmos.*, *119*, 12,674–12,688, doi:10.1002/2014JD021962.

Park, S. (2014), A Unified Convection Scheme (UNICON). Part I: Formulation, *J. Atmos. Sci.*, *71*(11), 3902–3930, doi:10.1175/JAS-D-13-0233.1.

Piriou, J.-M., J.-L. Redelsperger, J.-F. Geleyn, J.-P. Lafore, and F. Guichard (2007), An ppproach for convective parameterization with memory: Separating microphysics and transport in grid-scale equations, *J. Atmos. Sci.*, *64*(11), 4127–4139, doi:10.1175/2007JAS2144.1.

Powell, S. W., and R. A. Houze (2013), The cloud population and onset of the Madden-Julian oscillation over the Indian Ocean during DYNAMO-AMIE, *J. Geophys. Res. Atmos.*, *118*, 11, 979–11, 995, doi:10.1002/2013JD020421.

Purdom, J. F. W. (1976), Some uses of high-resolution GOES imagery in the mesoscale forecasting of convection and its behavior, *Mon. Weather Rev.*, *104*(12), 1474–1483, doi:10.1175/1520-0493(1976)104<1474:SUOHRG>2.0.CO;2.

Purdom, J. F. W., and K. Marcus (1982), Thunderstorm trigger mechanisms over the southeast United States, paper presented at 12th Conference on Severe Local Storms, AMS, San Antonio, Tex.

Qian, L., G. S. Young, and W. M. Frank (1998), A convective wake parameterization scheme for use in general circulation models, *Mon. Weather Rev.*, *126*(2), 456–469, doi:10.1175/1520-0493(1998)126<0456:ACWPSF>2.0.CO;2.

Redelsperger, J.-L., F. Guichard, and S. Mondon (2000), A parameterization of mesoscale enhancement of surface fluxes for large-scale models, *J. Clim.*, *13*(2), 402–421, doi:10.1175/1520-0442(2000)013<0402:apomeo>2.0.co;2.

Rio, C., F. Hourdin, J. Y. Grandpeix, and J. P. Lafore (2009), Shifting the diurnal cycle of parameterized deep convection over land, *Geophys. Res. Lett.*, *36*, L07809, doi:10.1029/2008GL036779.

Rio, C., et al. (2013), Control of deep convection by sub-cloud lifting processes: The ALP closure in the LMDZ5B general circulation model, *Clim. Dyn.*, *40*(9-10), 2271–2292, doi:10.1007/s00382-012-1506-x.

Rotunno, R., J. B. Klemp, and M. L. Weisman (1988), A theory for strong, long-lived squall lines, *J. Atmos. Sci.*, *45*(3), 463–485, doi:10.1175/1520-0469(1988)045<0463:atfsll>2.0.co;2.

Rowe, A. K., and R. A. Houze, Jr. (2014), Cloud organization and growth during the transition from suppressed to active MJO conditions, *J. Geophys. Res.*

Rowe, A. K., and R. A. Houze (2014a), Microphysical characteristics of MJO convection over the Indian Ocean during DYNAMO, *J. Geophys. Res. Atmos.*, *119*, 2543–2554, doi:10.1002/2013jd020799.

Schlemmer, L., and C. Hohenegger (2014), The formation of wider and deeper clouds as a result of cold-pool dynamics, *J. Atmos. Sci.*, *71*(8), 2842–2858, doi:10.1175/JAS-D-13-0170.1.

Terai, C. R., and R. Wood (2013), Aircraft observations of cold pools under marine stratocumulus, *Atmos. Chem. Phys.*, *13*(19), 9899–9914, doi:10.5194/acp-13-9899-2013.

Thompson, G., P. R. Field, R. M. Rasmussen, and W. D. Hall (2008), Explicit forecasts of winter precipitation using an improved bulk microphysics scheme. Part II: Implementation of a new snow parameterization, *Mon. Weather Rev.*, *136*(12), 5095–5115, doi:10.1175/2008MWR2387.1.

Tompkins, A. M. (2001), Organization of tropical convection in low vertical wind shears: The role of cold pools, *J. Atmos. Sci.*, *58*(13), 1650–1672, doi:10.1175/1520-0469(2001)058<1650:OOTCIL>2.0.CO;2.

Turner, D. D., et al. (2007), Thin liquid water clouds: Their importance and our challenge, *Bull. Am. Meteorol. Soc.*, *88*(2), 177–190, doi:10.1175/BAMS-88-2-177.

Wang, H., and G. Feingold (2009), Modeling mesoscale cellular structures and drizzle in marine stratocumulus. Part I: Impact of drizzle on the formation and evolution of open cells, *J. Atmos. Sci.*, *66*(11), 3237–3256, doi:10.1175/2009JAS3022.1.

Wilson, J. W., and W. E. Schreiber (1986), Initiation of convective storms at radar-observed boundary-layer convergence lines, *Mon. Weather Rev.*, *114*(12), 2516–2536, doi:10.1175/1520-0493(1986)114<2516:IOCSAR>2.0.CO;2.

Yoneyama, K., C. Zhang, and C. N. Long (2013), Tracking pulses of the Madden–Julian oscillation, *Bull. Am. Meteorol. Soc.*, *94*(12), 1871–1891, doi:10.1175/BAMS-D-12-00157.1.

Zeng, X., Q. Zhang, D. Johnson, and W. K. Tao (2002), Parameterization of wind gustiness for the computation of ocean surface fluxes at different spatial scales, *Mon. Weather Rev.*, *130*(8), 2125–2133, doi:10.1175/1520-0493(2002)130<2125:POWGFT>2.0.CO;2.

Zipser, E. J. (1977), Mesoscale and convective-scale downdrafts as distinct components of squall-line structure, *Mon. Weather Rev.*, *105*(12), 1568–1589, doi:10.1175/1520-0493(1977)105<1568:MACDAD>2.0.CO;2.

Zuidema, P., Z. Li, R. J. Hill, L. Bariteau, B. Rilling, C. Fairall, W. A. Brewer, B. Albrecht, and J. Hare (2011), On trade wind cumulus cold pools, *J. Atmos. Sci.*, *69*(1), 258–280, doi:10.1175/JAS-D-11-0143.1.

Zuluaga, M. D., and R. A. Houze (2013), Evolution of the population of precipitating convective systems over the equatorial Indian Ocean in active phases of the Madden-Julian oscillation, *J. Atmos. Sci.*, *70*(9), 2713–2725, doi:10.1175/jas-D-12-0311.1.